

## Research Paper



# The complex shape of the outer edge of Saturn's B ring, as observed in Cassini occultation data

Richard G. French<sup>a,\*</sup>, Philip D. Nicholson<sup>b</sup>, Colleen A. McGhee-French<sup>a</sup>, Pierre-Yves Longaretti<sup>c</sup>, Matthew M. Hedman<sup>d</sup>, Joshua Colwell<sup>e</sup>, Essam A. Marouf<sup>f</sup>, Nicole Rappaport<sup>g,1</sup>, Sophia Flury<sup>h</sup>, Jolene Fong<sup>a</sup>, Ryan Maguire<sup>i</sup>, Glen Steranka<sup>a</sup>

<sup>a</sup> Department of Astronomy, Wellesley College, Wellesley, MA 02481, United States of America

<sup>b</sup> Department of Astronomy, Cornell University, Ithaca, NY 14853, United States of America

<sup>c</sup> Institut de Planétologie et d'Astrophysique de Grenoble, Grenoble, FR, France

<sup>d</sup> Department of Physics, University of Idaho, Moscow, ID 83844, United States of America

<sup>e</sup> Department of Physics, University of Central Florida, Orlando, FL 32816, United States of America

<sup>f</sup> Department of Electrical Engineering, San José State University, San José, CA 95192, United States of America

<sup>g</sup> Jet Propulsion Laboratory, Pasadena, CA 91109, United States of America

<sup>h</sup> Department of Astronomy, University of Massachusetts, Amherst, MA 01003, United States of America

<sup>i</sup> Department of Mathematics, Dartmouth College, Hanover, NH 03755, United States of America

## ARTICLE INFO

**Keywords:**  
Occultations  
Planets  
Rings  
Dynamics

## ABSTRACT

We determine the time-variable shape of the outer edge of Saturn's B ring using the complete set of *Cassini* radio and stellar occultation data obtained between mid-2005 and the End-of-Mission in late 2017, considerably expanding the range and number of individual ring edge measurements used in previous analyses (Spitale and Porco, 2010; Nicholson et al., 2014a). During this 12-year interval, the dominant  $m = 2$  pattern driven by the Mimas 2:1 inner Lindblad resonance completed just over two rotations relative to Mimas, with a circulation period of 5.362 yr, while its radial amplitude varied from a minimum of 4 km to a maximum of 71 km. This circulation pattern has remained essentially unchanged over the full period of the observations. We confirm the existence of four additional perturbations with azimuthal wavenumbers  $m=1, 3, 4$  and 5 and mean amplitudes ranging from 5 to 24 km, which we interpret as normal or edge modes, possibly triggered by viscous overstabilities in the dense B ring (Borderies et al., 1985; Longaretti, 2018). Fits of a simple WKB model to the observed pattern speeds of the edge modes with  $m \neq 1$  suggest an average surface mass density in the outer 30 km of the B ring of  $\sim 100 \text{ g cm}^{-2}$ , somewhat greater than the 50–70  $\text{g cm}^{-2}$  inferred from density and bending waves in most other regions of this ring (Hedman and Nicholson, 2016). The  $m = 1$  mode, which extends further into the B ring, yields a more typical value of 60  $\text{g cm}^{-2}$ . Surprisingly, all four of these modes exhibit significant librations in their amplitudes and phases, with periods between 2.3 and 8.6 yr and amplitudes of 1.6 to 7.4 km. The origin of these librations is unknown and it is unclear if they are truly periodic and will maintain their amplitudes, periods, and phases over timescales of centuries. Their frequencies do not match those expected for interference between edge modes with varying numbers of radial nodes. Instead, they may represent periodic oscillations in the amplitudes of individual normal modes or nonlinear, non-resonant coupling between normal modes with different values of  $m$ , leading to long-term quasi-periodic variations in the mode amplitudes.

## 1. Introduction

The outer edge of Saturn's B ring – which is also the inner edge of the Cassini Division – coincides with the strongest satellite resonance in the rings: the 2:1 inner Lindblad resonance with Mimas (Tiscareno

and Harris, 2018). Although the likely connection between satellite resonances and the location of the Cassini Division was recognized in the 19th century (Kirkwood, 1866), if not earlier, the modern understanding of this phenomenon is due to Goldreich and Tremaine (1978), who pointed out that the torque exerted by Mimas on the ring

\* Corresponding author.

E-mail address: [rfrench@wellesley.edu](mailto:rfrench@wellesley.edu) (R.G. French).

<sup>1</sup> Retired.

at this resonance is probably large enough to counteract the outward transport of angular momentum through the B ring due to viscous interactions between the ring particles. As a result, the ring material is prevented from spreading radially beyond the resonance, and the edge of the B ring is effectively held in balance. A consequence of this picture is that Mimas should force significant perturbations on the orbits of ring particles near the resonance, resulting in a 2-lobed radial pattern that is expected to rotate at the same angular velocity as the satellite, or approximately one-half of the local Keplerian rate. Such a perturbation was in fact observed in *Voyager* observations of the rings in 1980/81 (Porco et al., 1984), where it was found to agree fairly well with theoretical expectations: at that time, the observed radial amplitude of the ring edge was  $\sim 75$  km and one of the two radial minima was found to be aligned with Mimas to within a few degrees. The torque itself, like the tidal torque exerted on the Earth's rotation by the Moon, arises from the interaction between this radial distortion of the ring streamlines and the gravitational potential of Mimas, and thus scales as the square of Mimas's mass. It is also proportional to the small phase lag in the ring's response relative to Mimas. For a recent discussion of the dynamics involved, as well as several as-yet-unanswered questions about this process, the reader is directed to the review by Longaretti (2018).

A similar situation occurs in the A ring, where another strong resonance appears to confine the outer edge of this ring against a similar tendency to spread radially. A revised calculation of the overall torque balance for both the A and B rings, taking into account the effects of additional satellite resonances, was made by Tajeddine et al. (2017), leading to updated estimates of the radial viscosity profiles across both rings.

With the advent of data from the *Cassini* spacecraft, it became possible to revisit the question of the shapes of the outer edges of the A and B rings, and to characterize them with much greater fidelity than was possible with the more limited *Voyager* observations. This problem was tackled using azimuthal mosaics of images acquired with *Cassini*'s Imaging Science Subsystem (ISS) during the initial years of the mission and by combining data from several dozen radio and stellar occultations observed by the Radio Science Subsystem (RSS) and the Visual and Infrared Imaging Spectrometer (VIMS). Spitale and Porco (2009) used ISS data to study the shape of the A ring's outer edge, while that of the B ring was analyzed by Spitale and Porco (2010), based on data taken between 2005 and 2009. Hedman et al. (2010) investigated the kinematics of the B ring edge using VIMS occultations between 2005 and 2008, while (French et al., 2010) carried out a similar study using a smaller set of RSS occultations from 2005.

As a result of these investigations, it was established that the shape of the B ring's edge, in particular, is remarkably complex. There are not one but two 2-lobed patterns, with similar radial amplitudes of approximately 35 km but rotating at slightly different angular rates. The slower of the two modes is that forced by Mimas, while the faster is a free normal mode (defined more precisely below). The result is that the two patterns beat against one another, alternately adding constructively and then almost canceling each other out (Hedman et al., 2010). Fits to a somewhat longer span of *Cassini* occultation data showed that the beat period is 5.42 yrs, with the overall  $m = 2$  amplitude reaching a maximum of 71 km and a minimum of 3 km (Nicholson et al., 2014a). During this cycle, the  $m = 2$  pattern was actually found to rotate through  $360^\circ$  relative to Mimas, instead of remaining aligned with the satellite as had been predicted (Spitale and Porco, 2010). Radial minima are anti-aligned with Mimas at the times of minimum amplitude, which occurred during the *Cassini* mission in 2006.80, 2012.24 and 2017.69. In addition to this circulating  $m = 2$  pattern, there is a slowly-rotating  $m = 1$  perturbation (equivalent to a precessing Keplerian ellipse) with an amplitude of  $\sim 20$  km and a rapidly-rotating  $m = 3$  pattern with an amplitude of  $\sim 10$  km. Evidence was later found for smaller-amplitude patterns with  $m = 4$  and  $m = 5$  (Nicholson et al., 2014a). These non-resonant perturbations with  $m = 1, 3, 4$  and  $5$ , as

well as the free mode with  $m = 2$ , are thought to represent normal modes trapped in resonant cavities near the ring's edge (Spitale and Porco, 2010; Nicholson et al., 2018).

In the present paper we return to the question of the shape of the B ring's outer edge, now armed with the complete set of *Cassini* radio and stellar occultation data obtained between mid-2005 and the End-of-Mission in late-2017. In addition to data from the RSS and VIMS experiments, we use stellar occultation data obtained by the Ultraviolet Imaging Spectrometer (UVIS), for a total of 294 measurements.

Our goals are:

- To characterize the forced  $m = 2$  mode and its phase lag relative to Mimas, with the hope of testing the resonant confinement model of Goldreich and Tremaine (1978).
- To determine the amplitudes and character of the normal modes with  $m = 1, 2, 3, 4$  and  $5$  and to model their librations. We explore three possible dynamical explanations for the observed time variability of the detected modes: (i) true physical oscillations of their amplitudes and phases, (ii) apparent oscillations due to the beating of separate normal modes with the same value of  $m$  but different numbers of radial nodes and (iii) quasi-periodic changes in amplitude and phase on decadal timescales as a consequence of nonlinear and non-resonant coupling between excited modes with different values of  $m$ .
- To search for additional, weaker perturbations that may shed further light on how this complex region works.

We have previously presented the results of a similar investigation of the outer edge of the A ring, using the same occultation data set (Nicholson et al., 2023).

Our presentation is organized as follows: In Section 2 we outline the dynamical model used to fit the occultation data, which are themselves summarized in Section 3. The numerical codes used for orbit fitting and frequency scanning are reviewed in Section 4. In Section 5 we update the fits published by Nicholson et al. (2014a), using the expanded *Cassini* data set. Our new results are presented in Section 6, and in Section 7 we discuss their implications for the surface mass density and viscosity of the outer B ring. We summarize our key findings and open questions in Section 8.

## 2. Dynamical model

Underlying all of the orbital fits in this paper is a common kinematic model for the  $m$ -lobed radial perturbation of a ring edge appropriate to both a Lindblad resonance due to an external satellite and to free normal modes of oscillation, also known as edge modes and described by Nicholson et al. (2018). Our notation follows closely that used in our previous papers, in particular (Nicholson et al., 2014a), Nicholson et al. (2014b) and French et al. (2016), so that the fit parameters obtained here may be compared directly with the corresponding values given there. The radial perturbation in a ring streamline due to such a mode can be written as a function of inertial longitude  $\lambda$  (measured from the ascending node of Saturn's equator on Earth's equator of J2000) and time  $t$  in the form

$$\Delta r(m, \lambda, t) = -A_m \cos[m(\lambda - \Omega_p(t - t_0) - \delta_m)], \quad (1)$$

where  $A_m$  and  $\delta_m$  are the mode's radial amplitude and phase, respectively, and  $\Omega_p$  is its angular rotation rate or pattern speed. Geometrically, the angle  $\delta_m$  is the inertial longitude of one of the pattern's  $m$  minima at the reference time  $t_0$ . In the residual plots shown below we use the corotating longitude  $\theta = \lambda - \Omega_p(t - t_0) - \delta_m$ , so the angular argument becomes simply  $m\theta$ . For a freely-precessing normal mode, the pattern speed is expected to be very close to that of a first-order  $m : m - 1$  Lindblad resonance located at the mean radius of the streamline (French et al., 1991), or

$$\Omega_p = [(m - 1)n + \dot{\omega}_{\text{sec}}]/m, \quad (2)$$

where  $n$  is the local orbital angular velocity and  $\dot{\omega}_{\text{sec}}$  is the local apsidal precession rate due to the planet's zonal gravity harmonics.<sup>2</sup> In general, the integer  $m$  can be either positive or negative, corresponding to ILR-type modes with  $\Omega_p < n$  or OLR-type modes with  $\Omega_p > n$ , respectively. (This terminology refers to an inner or outer Lindblad resonance, which the normal mode perturbations strongly resemble.) The former are expected to occur at the outer edges of rings, whereas the latter should be found at inner edges, as discussed in Nicholson et al. (2014b) and French et al. (2016) and reviewed by Nicholson et al. (2018). At the outer edge of the B ring, only ILR-type modes are expected (*i.e.*,  $m > 0$ ). A normal mode with  $m = 1$  is equivalent to a freely-precessing Keplerian ellipse, with  $\Omega_p = \dot{\omega}_{\text{sec}}$ , the apsidal precession rate, and  $\delta_1 = \varpi_0$ , the longitude of pericenter at  $t = t_0$ .

In the case of perturbations by an external satellite,  $\Omega_p$  is determined by the relevant term in the satellite's gravitational potential. For the B ring edge, the resonant perturbations are due to the Mimas 2:1 inner Lindblad resonance for which  $m = 2$  and  $\Omega_p = n_{\text{Mimas}}$ . Here, we expect that  $\delta_2 = \lambda_{\text{Mimas}}^0$ , the mean longitude of Mimas at  $t = t_0$ , although in our fits we allow for a small offset  $\delta\lambda$  to account for the anticipated phase lag between the radial minimum and the direction towards the satellite. (A positive value of  $\delta\lambda$  means that the radial minimum leads Mimas in longitude.)

In the current paper, we shall also be concerned with modes whose amplitude and phase oscillate, or *librate* about their average values. Such oscillations could arise in several different ways, as outlined below. To handle this situation we generalize Eq. (1) to the form

$$\begin{aligned} \Delta r(m, \lambda, t) &= -A_m \cos(m\theta - \phi_L) \\ &= -A_m \cos(m[\lambda - \Omega_p(t - t_0) - \delta_m] - \phi_L), \end{aligned} \quad (3)$$

where both  $A_m$  and  $\phi_L$  are slowly-varying functions of time. Following the standard model used to describe secular perturbations of asteroid or satellite orbits (Murray and Dermott, 1999), or that introduced by Hedman et al. (2010) and Spitale and Porco (2010) to describe resonant librations associated with the Mimas 2:1 ILR, we write  $A_m = ae$  and describe these periodically-varying parameters in terms of the Cartesian quantities  $h = e \cos(\phi_L)$  and  $k = e \sin(\phi_L)$  via the expressions

$$\begin{aligned} h &= e_0 + e_1 \cos[\Omega_L(t - t_0) - \delta_L] \\ k &= e_1 \sin[\Omega_L(t - t_0) - \delta_L], \end{aligned} \quad (4)$$

where  $e_0$  and  $e_1$  are constants,  $\Omega_L$  is the libration frequency and  $\delta_L$  is a constant specifying the phase of the libration.<sup>3</sup> Geometrically, the vector  $(h, k)$  moves around a circle of radius  $e_1$  at an angular rate  $\Omega_L$ , with the center of the circle offset from the origin by an amount  $e_0$  along the  $+h$ -axis. In the context of secular or resonant perturbations,  $e_0$  is referred to as the forced eccentricity and  $e_1$  as the free or proper eccentricity. In the present situation,  $ae_0$  and  $ae_1$  simply represent the average and variable components of the mode's amplitude  $A_m$ . In terms of  $h(t)$  and  $k(t)$ , the instantaneous values of  $e$  and  $\phi_L$  are given by

$$\begin{aligned} e &= \sqrt{h^2 + k^2} \\ \phi_L &= \tan^{-1}(k/h). \end{aligned} \quad (5)$$

Similar expressions are given by Hedman et al. (2010) in Eqs. (35–40) and by Spitale and Porco (2010) in Eqs. (6 & 11); see also Fig. 4 in Spitale and Porco (2010) for a graphical representation of the motion. From Eq. (4) we see that the mode amplitude  $A_m = ae$  is a maximum when  $\phi_L = 0$  and the angle  $\Omega_L(t - t_0) - \delta_L$  is zero, modulo  $2\pi$ , or when

$$t - t_0 = \delta_L/\Omega_L + 2\pi k/\Omega_L, \quad (6)$$

<sup>2</sup> Expressions for  $n$  and  $\dot{\omega}_{\text{sec}}$  accurate to order  $J_6$  are given by Nicholson et al. (2014b), Eqs. (3–8) and Nicholson et al. (2018), Eqs. (26 & 27).

<sup>3</sup> For simplicity, we refer to this motion as *libration*, implying an oscillation in  $\phi_L$ , but this can also include the case where  $e_1 > e_0$ , when the angle  $\phi_L$  actually circulates continuously through  $360^\circ$ .

where  $k$  is any integer.

As noted above, librations of this form can arise in several distinct ways, as outlined by Longaretti (2023). In the first and simplest scenario, the amplitude and phase of a single mode oscillate about mean values given by  $Ae_0$  and  $\delta_m$ , perhaps due to a viscously-induced overstability as suggested by Borderies et al. (1985). In this case the libration frequency is a function of both the surface mass density of the ring  $\sigma$  and of its effective viscosity  $\nu$  (Longaretti, 2018). A second scenario was introduced by Spitale and Porco (2010), who showed that such a model for a ring edge is mathematically equivalent to a superposition of two independent normal modes with the same value of  $m$ , radial amplitudes  $ae_0$  and  $ae_1$  and slightly different pattern speeds  $\Omega_0$  and  $\Omega_1$ . Geometrically, one may imagine two independent normal modes, one with amplitude  $ae_0$  rotating at a rate  $\Omega_0$  and the other with amplitude  $ae_1$  and angular frequency  $\Omega_1$ , combining to produce a single, pulsating, rotating perturbation with a beat frequency equal to  $|m(\Omega_1 - \Omega_0)|$  and an amplitude that varies from a minimum of  $a|e_0 - e_1|$  to a maximum of  $a(e_0 + e_1)$ . In this case we somewhat arbitrarily designate the larger-amplitude mode as 'mode 0' and choose  $\Omega_p = \Omega_0$ . The corresponding libration frequency is then given by

$$\Omega_L = m(\Omega_1 - \Omega_0). \quad (7)$$

(The factor of  $m$  arises because each mode has  $m$  radial minima and maxima.) A third scenario may arise if nonlinear interactions between normal modes with *different* values of  $m$  lead to the exchange of energy between the modes and thus result in slow and unpredictable variations in their amplitudes. In this case, the librations are unlikely to be strictly periodic, but they may appear so over a short span of observations.

There are thus at least two dynamically distinct situations that can arise, one in which a single mode oscillates in amplitude and phase and the other in which two stable modes with the same value of  $m$  and similar pattern speeds interfere to produce a beating pattern. These two scenarios are indistinguishable when only the shape of a single ring streamline – such as a ring edge – is analyzed, so that in practice we do not make any distinction between them in analyzing the occultation measurements of the ring edge. But if the radial distribution of eccentricity across the perturbed region of the ring could be assessed, and its temporal variation established, then these two situations might look quite different. We return to these alternate possibilities in Section 7.1.

For some values of  $m$  we have found it necessary to introduce more than one librational term, replacing Eq. (4) by the more general expression:

$$\begin{aligned} h &= e_0 + \sum_{j=1}^n e_j \cos[\Omega_{L,j}(t - t_0) - \delta_{L,j}] \\ k &= \sum_{j=1}^n e_j \sin[\Omega_{L,j}(t - t_0) - \delta_{L,j}] \end{aligned} \quad (8)$$

where each librational term has its own frequency  $\Omega_{L,j}$  and phase  $\delta_{L,j}$ . Fig. 1 illustrates the overall eccentricity and phase for a mode with two libration terms, plotted in  $(h, k)$  space. The radial line from the origin to the center of the larger circle of length  $e_0$  is fixed, while the radius vectors of the two smaller circles (labeled  $e_1$  and  $e_2$ ) rotate at angular rates of  $\Omega_{L,1}$  and  $\Omega_{L,2}$ , respectively. (Note that this diagram shows just the variation in amplitude  $e$  and phase  $\phi_L$  of the mode, rather than the shape of the ring streamline itself, which is an  $m$ -lobed figure, or its orientation relative to inertial space, which is controlled by  $\Omega_p$  and  $\delta_m$ .) In this situation, we label the additional libration terms so that  $e_0 > e_1 > e_2$ , etc.

In general, a particular ring streamline may be perturbed simultaneously by several different normal modes, each with its own value of the azimuthal wavenumber  $m$ , and each of these modes can librate with one or more components, following Eq. (8). Such a model is specified by a set of free parameters given by the mean radius  $a$ , three parameters for the mean amplitude and phase for each mode ( $ae_0$ ,  $\Omega_p$ ,  $\delta_m$ ) and an additional three parameters for each libration ( $ae_j$ ,  $\Omega_{L,j}$ ,  $\delta_{L,j}$ ). A

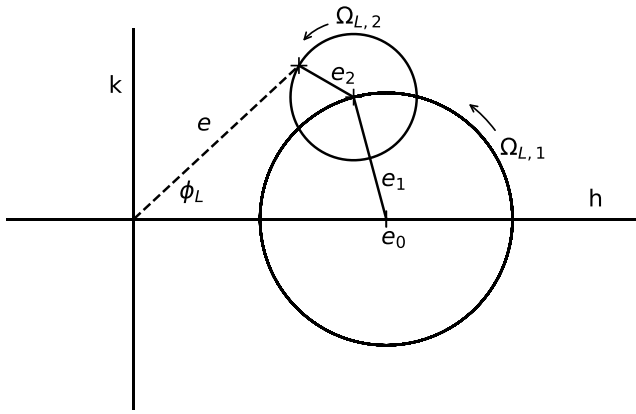


Fig. 1. Illustration of the time-varying eccentricity vector  $\{h, k\}$  for a mode with two libration terms and a mean amplitude  $ae_0$ . The two smaller circles have radii of  $e_1$  and  $e_2$  and rotate at angular rates of  $\Omega_{L,1}$  and  $\Omega_{L,2}$ , respectively. The instantaneous amplitude and phase of the mode are indicated by the dashed line and specified by  $ae$  and  $\phi_L$ .

Source: Adapted from Spitale and Porco (2010), Fig. 4.

particular mode has  $m$  lobes of radial amplitude  $A_m(t) = ae(t)$  with radial minima located at longitudes where  $m\theta = \phi_L$ , or at

$$\lambda_{\min}(t) = \Omega_p(t - t_0) + \delta_m + \phi_L(t)/m + 2\pi k/m, \quad (9)$$

where  $0 \leq k \leq m - 1$ . Geometrically, the pattern has a mean amplitude  $ae_0$  and rotates relative to inertial space at a mean rate  $\Omega_p$ , while oscillating in both amplitude and orientation at a frequency (or frequencies)  $\Omega_{L,j}$ .

### 3. Observations

The data used for this study come from a large set of *Cassini* ring occultations observed over the full course of the spacecraft's 2004–2017 orbital tour of the Saturn system.<sup>4</sup> Details of the relevant VIMS, UVIS, and pre-2012 RSS occultation observations are provided in Nicholson et al. (2014a,b) and French et al. (2010, 2016, 2017), and are not repeated here. A total of 305 measurements of the B ring edge radius were included, with 58 from RSS, 115 from VIMS and 132 from UVIS. Fully calibrated versions of the occultation data are available from NASA's Planetary Data System (PDS) Ring-Moon Systems Node.<sup>5</sup>

#### 3.1. Post-2011 RSS ring occultations

In addition to the above data sets, we have included post-2011 RSS occultation results that contributed significantly to the final tally of B ring measurements used for this work, and these deserve more detailed discussion.

Unlike stellar occultation observations, which require only modest processing from their raw form to obtain useful science results, raw RSS ring occultation observations are strongly affected by diffraction effects that must be removed in order to determine the intrinsic optical depth profiles of the rings (Marouf et al., 1986). The diffraction reconstruction relies on a highly accurate measurement of the radio signal's phase, which requires a very stable transmitted frequency from the spacecraft. In late 2011, the *Cassini* spacecraft's ultrastable oscillator (USO) failed, and the auxiliary onboard oscillator had inadequate frequency stability

<sup>4</sup> Although spacecraft imaging data have the advantage of revealing the continuous shape of the ring edge at discrete observing intervals (Spitale and Porco, 2010), the occultation data are more useful for quantifying the changes in shape over time, a key objective of this study.

<sup>5</sup> <https://pds-rings.seti.org/>

to allow for accurate diffraction reconstruction of ring occultations. Instead, a novel mode of two-way RSS occultation experiments was implemented in 2012. Rather than depending on a stable onboard frequency source for the spacecraft's transmitted signal, an uplink radio signal from an Earth-based Deep Space Network (DSN) antenna was transmitted to the spacecraft, where it was phase-locked, amplified and then retransmitted to the ground, preserving the hydrogen maser-based frequency stability of the original signal from the DSN.

A key complication is that the uplinked signal passed through the rings on the way to the spacecraft, resulting in a phase distortion preserved in the downlink signal. In effect, the observations retain a “double exposure” or “phase echo” associated with the diffraction pattern of the ring region traversed by the uplink signal, coadded to the diffraction phase of the downlink signal. This contamination of the final received phase during an RSS occultation experiment similarly affects atmospheric occultations, but in this case the use of multi-frequency observations can correct for the phase distortion and enable accurate retrieval of the vertical profile of the atmospheric structure (Schinder and colleagues, 2015).

For ring occultations, on the other hand, no general solution has yet been found to remediate the phase contamination that often results in badly distorted diffraction-corrected radial optical depth ring profiles. Under special circumstances, however, the observed diffraction pattern of specific ring features may be relatively unaffected by the uplink phase distortion. For example, it is possible to retrieve the intrinsic optical depth profile of an isolated narrow ringlet such as the F ring if the phase echo is sufficiently radially separated from the main diffraction signature of the downlink signal.

It is also possible, under the right geometric circumstances, to reconstruct the intrinsic sharp edge of a nearly opaque ring bounded by free space, such as the outer edges of the A and B rings. Fortunately, a significant fraction of the post-2011 RSS occultations had such favorable geometry. In the end, we were able to apply standard diffraction-reconstruction techniques (Marouf et al., 1986) to process the X-band (3.6 cm wavelength) observations at 1-km effective resolution and to obtain accurate measurements of the B ring outer edge from 24 of 41 post-USO-failure RSS occultations that intersected the B ring, expanding the available data for the post-2011 period of the *Cassini* orbital tour.

#### 3.2. Measuring the location of the B ring edge

As in our previous studies, we have included only high-SNR events with spatial resolution of 1 km or better that could be mapped onto an absolute radius scale with sub-km accuracy. For each such occultation that included the outer edge of the B ring, we fitted a logistic model curve to the radial optical depth profile of the edge to determine the corresponding midtime. Using a Saturn ring orbit model similar to Fit #1 in French et al. (2017) but augmented to include the full set of 2005–2017 *Cassini* occultation data, we determined the orbital radius, inertial longitude, and ring plane intercept time of each B ring edge measurement. These represent the fundamental observables for our B ring orbit fits. The typical uncertainty in an individual radius determination, including systematic effects, is well below 1 km. Post-fit RMS residuals of  $\sim 5$  km for our best B ring model fits greatly exceed this measurement uncertainty, and instead probably stem from complexities in the intrinsic shape of the B ring edge that are not captured by our kinematical models.

From preliminary orbit fits that included normal modes for  $m = 1$  through 5 and the  $m = 2$  mode forced by Mimas, we identified 11 of the 305 individual data points as having unacceptably large ( $>20$  km) post-fit residuals, corresponding to  $\sim 4$  standard deviations. These are listed in Table 1. Such outliers were a characteristic of our earlier B ring investigation (Nicholson et al., 2014a) and were also noted by Spitale and Porco (2010) in their analysis of imaging mosaics. They interpreted these large but localized radial disturbances in the B ring edge as evidence for the presence of massive bodies embedded within

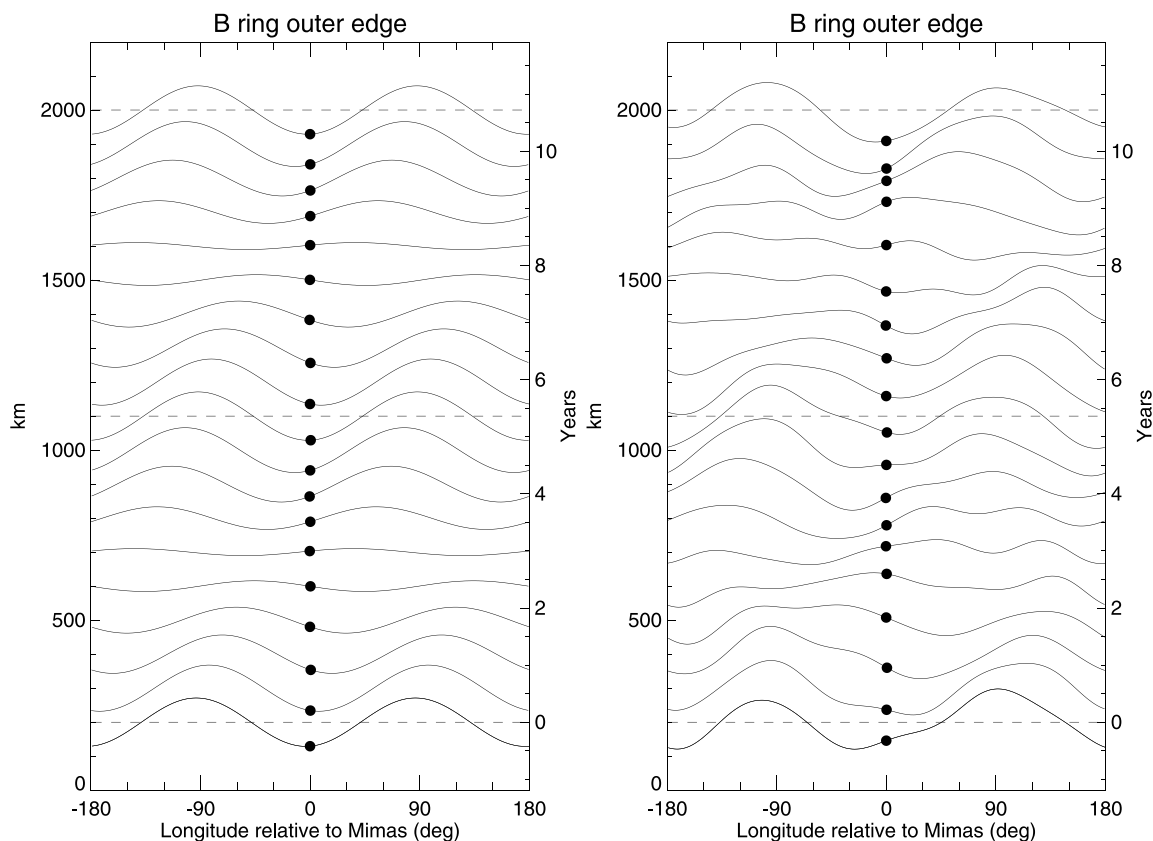


**Fig. 2.** Representative profiles of the B ring edge over two libration periods of the  $m = 2$  pattern, plotted in radius (on the left axis) and time (on the right axis) as a function of longitude relative to Mimas, whose position is indicated by the large filled circles. The left panel shows the  $m = 2$  mode only, while the right panel includes all five modes. The bottom profiles correspond to a time when the forced and free components of the  $m = 2$  mode are in phase (i.e.,  $\phi_L = 0$ ), so that the amplitude of the mode is at its maximum value. Successive profiles are shown at intervals of  $1/9$  of the  $m = 2$  libration period, and offset upwards by 100 km for clarity. Horizontal dashed lines mark successive  $m = 2$  libration periods of 5.354 yr.

**Table 1**  
Omitted measurements of the B ring edge with large post-fit residuals.

Occultation	UTC (observed)	$r_{\text{obs}}$ (km)	$r_{\text{model}}$ (km)	$dr$ (km)	$\lambda$ (deg)
RSS_013E_X14	2005 AUG 20 20:37:46.8732	117569.19	117548.78	20.40	79.57
UVIS_EpsCen065I	2008 APR 19 11:32:19.8837	117551.54	117518.50	33.04	204.26
VIMS_alpAur110E	2009 MAY 09 16:45:55.8991	117583.65	117614.00	-30.35	243.49
RSS_180I_X14_65	2013 JAN 31 13:48:24.4050	117585.38	117557.22	28.16	299.28
VIMS_2Cen194E	2013 JUL 08 21:30:05.0270	117555.40	117585.98	-30.57	248.19
RSS_196I_X65_65	2013 AUG 08 18:24:19.3052	117584.64	117545.15	39.49	228.88
UVIS_AlVir211I	2015 JAN 08 03:50:58.4312	117598.84	117627.00	-28.16	168.48
VIMS_alpSco238I	2016 JUL 19 13:45:57.5389	117557.58	117584.09	-26.51	233.76
RSS_236E_X43_14	2016 JUN 06 10:42:10.8061	117566.38	117594.51	-28.13	109.65
RSS_253E_X14_63	2016 DEC 19 20:40:19.1470	117581.59	117554.33	27.26	188.80
VIMS_alpOri277I	2017 JUN 04 22:40:28.7150	117598.39	117573.89	24.50	352.64

the B ring itself. We excluded this small number of outliers from our final data set because they unduly inflated the formal errors of the final fit parameters. The total number of data points used in our current fits is thus 294, or more than twice the 133 B ring edge measurements used by Nicholson et al. (2014a).

#### 4. Orbit determination

As in Nicholson et al. (2014a), we determine the best-fitting orbit model for the B ring edge using a straightforward and well-tested non-linear least squares procedure that minimizes the sum of squared differences between the observed and model radii,  $r_{\text{obs}}(\lambda, t)$  and  $r_{\text{mod}}(\lambda, t)$ , where

$$r_{\text{mod}}(\lambda, t) = a + \sum_{i=1}^M \Delta r(m_i, \lambda, t). \quad (10)$$

Here,  $a$  is the semimajor axis of the B ring's outer edge and the summation is performed over the radial perturbations  $\Delta r(m, \lambda, t)$  given by Eq. (3) associated with the  $M$  separate modes (i.e., values of  $m$ ) for a given ring model. The goodness of each fit is characterized by the root-mean-square residual per degree of freedom  $\sigma$ , where we define

$$\sigma^2 = \frac{1}{N - N_p} \sum_{i=1}^N [r_{\text{obs}}(\lambda, t) - r_{\text{mod}}(\lambda, t)]^2. \quad (11)$$

Here,  $N$  is the number of independent fitted data points and  $N_p$  is the number of parameters in the fit. We approach our search for possible normal modes by first fitting a circular model to the data, forming the residuals, and then scanning over a range of pattern speeds  $\Omega_p$  in the vicinity of the predicted value for the mean radius, based on Eq. (2) and candidate wavenumbers from  $m = 1$  to  $m = 20$  for ILR-type perturbations. For each assumed value of  $m$  and  $\Omega_p$ , we solve for the best-fitting amplitude  $A_m$  and phase  $\delta_m$  and record the value of the

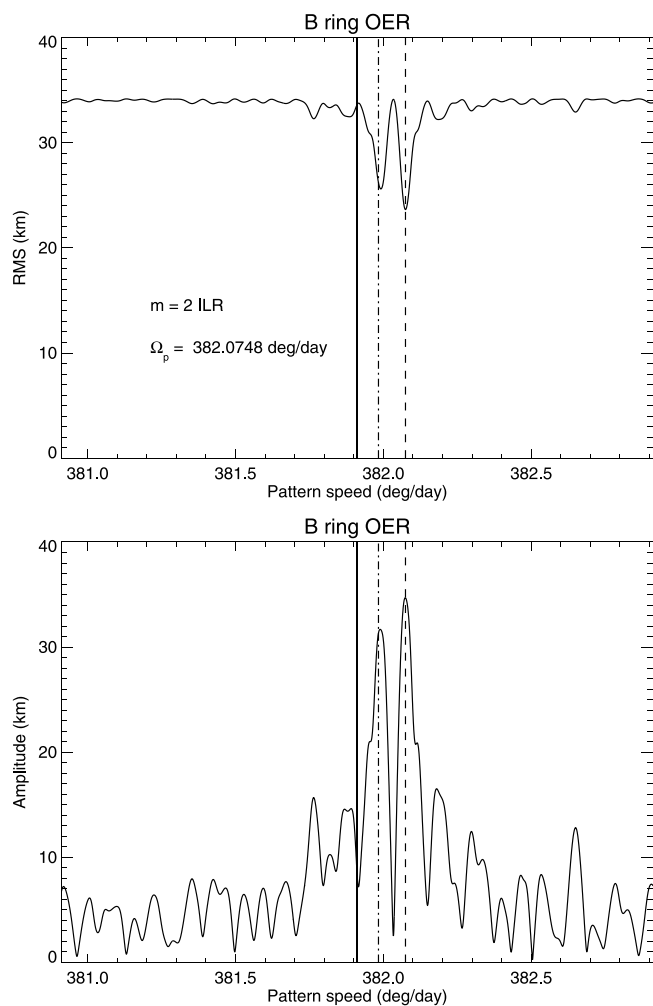


**Fig. 3.** A scan in pattern speed for  $m = 2$  normal modes, after removing the signatures of all other modes listed in Table 2. The upper panel shows the root-mean-square residual of the fit  $\sigma$  as the pattern speed is scanned across the expected value, while the lower panel shows the fitted radial amplitude of the mode  $A_2$  for the same scan. Note the detection of significant power at two different pattern speeds,  $381.984^\circ \text{ d}^{-1}$  and  $382.075^\circ \text{ d}^{-1}$ , with radial amplitudes of 31 and 36 km. The solid vertical line indicates the predicted value of  $\Omega_p$  at the mean radius of the B ring's outer edge, or  $381.913^\circ \text{ d}^{-1}$ , while the dashed line highlights the value of  $\Omega_p$  for the strongest peak in the scan, with a minimum  $\sigma = 23.9$  km. The dot-dashed line indicates the average mean motion of Mimas of  $381.9835^\circ \text{ d}^{-1}$ .

RMS residual  $\sigma$ . We then add the strongest of the detected modes to the kinematical model of the B ring edge, form a new set of residuals, and repeat the frequency scanning process to search for additional modes. With the addition of successive normal modes, the post-fit value of  $\sigma$  is reduced and the sensitivity to weaker modes and possible libration terms is increased.

Once a preliminary set of global normal modes has been identified, we divide the dataset into smaller segments and examine the observed variation in amplitude for each mode over the 13 yr time span of the observations. Based on these shorter-period fits, we solve for the characteristics of any necessary libration terms, as described by Eq. (4) or (8), that can best account for the long-term trends seen in the mode amplitudes. In the next two sections, we turn to a description of the results of this process.

## 5. Reference model

Because the *Cassini* occultation data set has more than doubled in size from that used by Nicholson et al. (2014a) — 294 observations

**Table 2**

Reference model fit to *Cassini* data.

Parameter	Symbol	Value
mean radius	$a$ (km)	$117570.32 \pm 0.42$
Forced $m = 2$ mode	$ae_0$ (km)	$33.20 \pm 0.63$
	$\Omega_p$ ( $^\circ \text{ d}^{-1}$ )	$381.9843 \pm 0.0005$
$m = 2$ libration	$\delta_2$ ( $^\circ$ )	$346.83 \pm 0.73$
	$ae_1$ (km)	$39.40 \pm 0.64$
	$\Omega_L$ ( $^\circ \text{ d}^{-1}$ )	$0.1841 \pm 0.0008$
	$P_L$ (yr)	$5.354 \pm 0.023$
	$\delta_L$ ( $^\circ$ )	$96.07 \pm 1.86$
Epoch	$t_0$	UTC 2008 Jan 1 12:00
RMS residual	$\sigma$ (km)	6.98
# data	N	294
Fit ID		ringfit_v1.8.Sa025S-CMF-V6980-RF-B95

$m$	$A_m$ (km)	$\Omega_p$ ( $^\circ \text{ d}^{-1}$ )	$\delta_m$ ( $^\circ$ )
1	$22.35 \pm 0.59$	$5.0814 \pm 0.0011$	$69.34 \pm 2.14$
3	$9.54 \pm 0.60$	$507.7185 \pm 0.0008$	$24.48 \pm 1.53$
4	$8.38 \pm 0.58$	$570.5293 \pm 0.0008$	$6.91 \pm 1.43$
5	$5.87 \pm 0.60$	$608.2073 \pm 0.0008$	$67.98 \pm 1.59$

now vs 133 in the previous work — and also doubled in duration (thirteen vs six years), our first step is to redo the best fit in Nicholson et al. (2014a) using all the currently-available *Cassini* occultation data. For this purpose, we compare our new results with those of Fit 11 in Nicholson et al. (2014a), as described in their Table 5. Note that both fits exclude the relatively small number of pre-*Cassini* observations, derived from *Voyager* and Earth-based occultations. Experiments show that while the longer time baseline provided by these earlier data improves the accuracy with which pattern speeds can be determined, the much sparser temporal coverage also leads to problems with aliasing and multiple solutions.

This fit, which we refer to henceforth as our reference model, includes – in descending order of importance – a circulating  $m = 2$  mode, a free eccentricity (i.e., an  $m = 1$  mode), and fixed-amplitude normal modes with  $m = 3, 4$  and  $5$ . The  $m = 2$  mode has two components: a forced eccentricity (which we denote as  $e_0$ ) due to the Mimas 2:1 ILR and a free eccentricity (denoted as  $e_1$ ) that we interpret as a normal mode. Departing slightly from Fit 11 in Nicholson et al. (2014a), where we fixed  $\Omega_p$  for the forced  $m = 2$  mode at the average value of Mimas's mean motion in 2005–2010 and fixed the corresponding phase  $\delta_2$  to be Mimas's mean longitude at our reference time, in the current fit we permit both parameters to float, with *a priori* values corresponding to the Mimas resonance. (Alternate fits in which  $\Omega_p$  and  $\delta_2$  were fixed at their expected values were almost indistinguishable.) Table 2 presents the results of this reference fit, which we will use below as a standard against which to compare our new fits that include additional librations.

A comparison with the parameters of Fit 11 of Nicholson et al. (2014a) reveals the following:

- The mean radius of the B ring edge is almost unchanged at  $a = 117,570.32 \pm 0.42$  km. This is  $\sim 14.5$  km exterior to the nominal location of the Mimas 2:1 ILR at  $a_{\text{res}} = 117,555.8$  km (Spitale and Porco, 2010).
- The minimum post-fit root-mean-square residual per degree of freedom is 6.98 km, comparable to but slightly lower than the 7.81 km obtained for Fit 11. This remains much larger than the typical measurement errors, which are well under 1 km for this sharp, well-defined edge, and also much larger than post-fit residuals obtained for most other sharp-edged features in the Cassini Division (French et al., 2016), suggesting that significant unmodeled radial perturbations remain.
- The larger component of the  $m = 2$  mode is again the free (or normal) mode, whose amplitude has increased from 37.1 km to  $ae_1 = 39.40 \pm 0.64$  km, while the forced component due to the Mimas resonance is almost unchanged at  $ae_0 = 33.20 \pm$

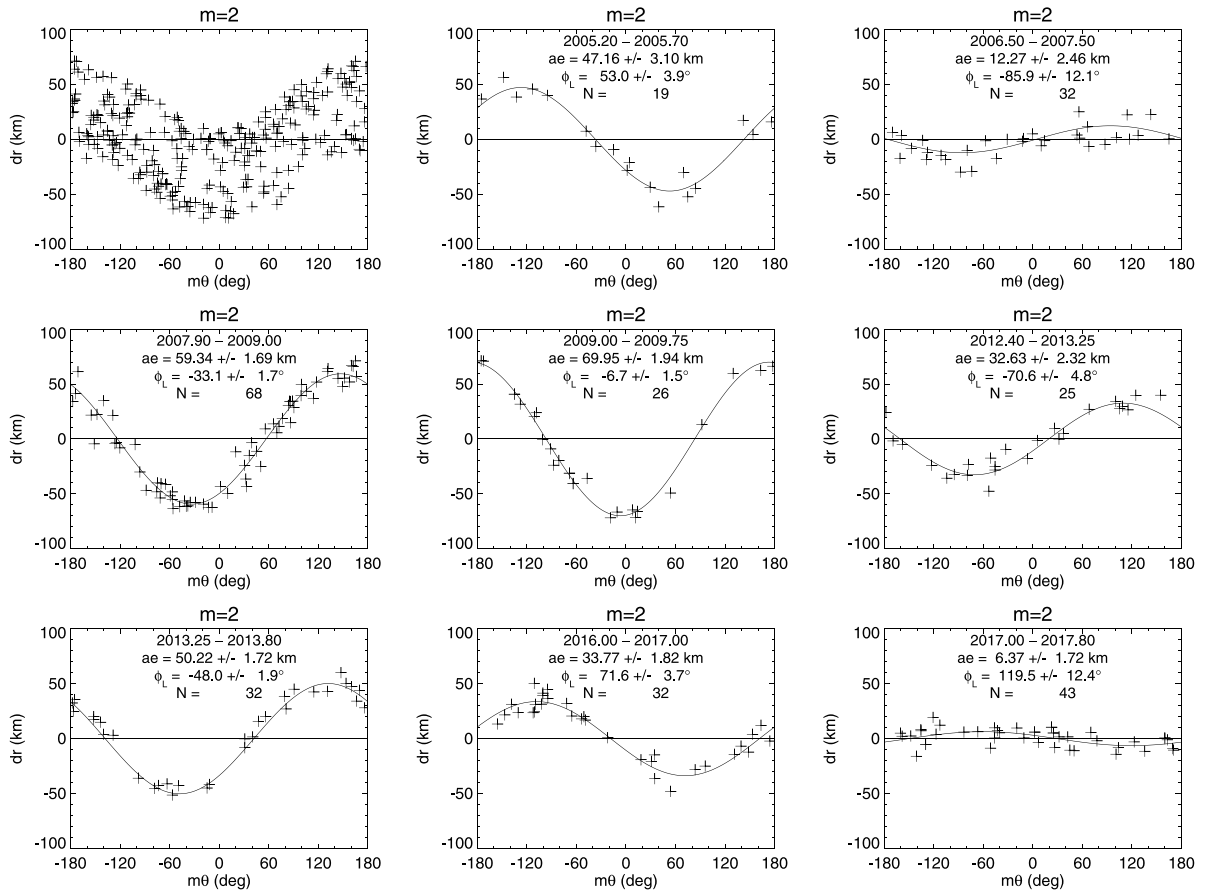


Fig. 4. Radius residuals from our reference model when the free and forced  $m = 2$  terms are set to zero, plotted as a function of  $m\theta$ , for  $\Omega_p = 381.9843^\circ \text{ d}^{-1}$ . The upper left panel shows the full set of observations, with substantial scatter. The observations are divided into eight different time intervals in the remaining panels, showing substantial systematic variations in the amplitude and phase of the  $m = 2$  pattern over time. See text for details of the model fit results included in these panels.

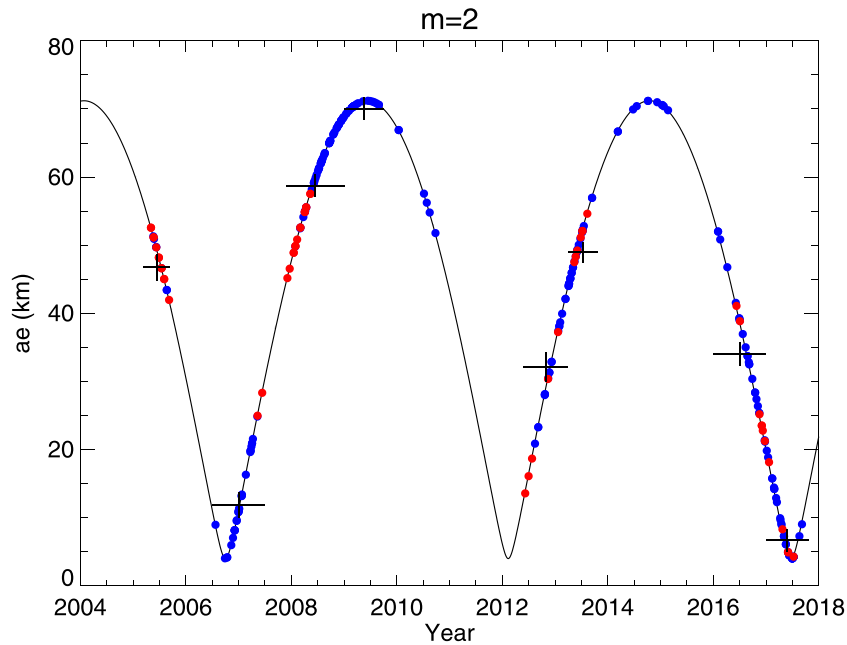
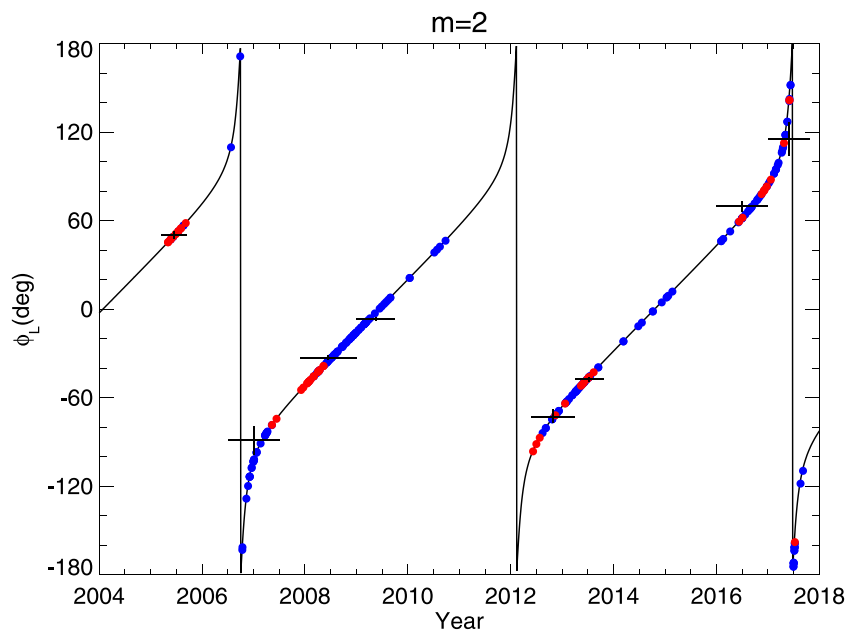


Fig. 5. The variation in the  $m = 2$  amplitude  $ae$ , as computed from the reference model. Blue dots mark the model values of  $ae$  at times of individual stellar occultation observations, and the red symbols mark RSS observations. Fitted average values over the eight selected intervals in Fig. 4 are shown as large '+' symbols, with the vertical extent showing the formal uncertainty in the amplitude and the horizontal extent representing the time span of data used in each fit. (For interpretation of the references to color in this figure legend, the reader is referred to the web version of this article.)



**Fig. 6.** The variation in the  $m = 2$  libration phase  $\phi_L$ , as computed from the reference model. Note the highly non-uniform rate  $d\phi_L/dt$  as the time-varying eccentricity vector sweeps rapidly through its minimum range. As in Fig. 5, blue symbols mark the model values at times of stellar occultation observations and red symbols mark RSS observations. The fitted average phase values over the eight selected intervals in Fig. 4 are shown as large '+' symbols, with the vertical extent showing the formal uncertainty in the average phase over the interval and the horizontal extent representing the time span of data used in each fit. (For interpretation of the references to color in this figure legend, the reader is referred to the web version of this article.)

0.63 km. The fitted pattern speed for the forced component is  $\Omega_p = 381.9843 \pm 0.0005^\circ \text{ d}^{-1}$ , very close to the average mean motion of Mimas of  $\sim 381.986^\circ \text{ d}^{-1}$  during the period of the *Cassini* mission. The libration frequency remains almost unchanged at  $\Omega_L = 0.1841 \pm 0.0008^\circ \text{ d}^{-1}$  with a corresponding period  $P_L = 5.354 \pm 0.023 \text{ yr}$ . Geometrically, this means that the angle  $\phi_L$  circulates through  $360^\circ$  once every libration period ( $= 2\pi/\Omega_L$ ) and that the minor axis of the  $m = 2$  pattern rotates through  $360^\circ$  with respect to Mimas once every two libration periods, or  $\sim 10.7 \text{ yr}$  (see Eq. (9)). (See Section 7.2 for further discussion of the significance of this point and of the phase lag of the forced component.)

- Next in importance is the  $m = 1$  mode, or free eccentricity, which has increased somewhat in amplitude from  $20.4$  to  $22.35 \pm 0.59 \text{ km}$ , but which has maintained its pattern speed almost unchanged at  $5.0814 \pm 0.0011^\circ \text{ d}^{-1}$ .
- The  $m = 3$  mode, on the other hand, has decreased in amplitude from  $12.5$  to  $9.54 \pm 0.60 \text{ km}$ , while increasing its pattern speed by  $\sim 6\sigma$  to  $507.7185 \pm 0.0008^\circ \text{ d}^{-1}$ .
- Next is the  $m = 4$  mode, which has increased significantly in amplitude from  $5.9$  to  $8.38 \pm 0.58 \text{ km}$ , while increasing its pattern speed by  $\sim 4\sigma$  to  $570.5293 \pm 0.0008^\circ \text{ d}^{-1}$ .
- Lastly we have the  $m = 5$  mode, which is almost unchanged in amplitude at  $5.87 \pm 0.60 \text{ km}$  and in pattern speed at  $608.2073 \pm 0.0008^\circ \text{ d}^{-1}$ .

To illustrate the reference model, Fig. 2 shows snapshots of the co-added modes over a period of two libration cycles, in the form of profiles of the radial displacement of the B ring edge as a function of longitude relative to Mimas. Note that the  $m = 2$  pattern slowly circulates relative to Mimas, with an amplitude of  $\sim 73 \text{ km}$  when its forced and free components are in phase but only  $\sim 6 \text{ km}$  when the two components are out of phase by  $\pi$ .

## 6. Results

Having updated the mode fits of Nicholson et al. (2014a) with the more complete *Cassini* data set, we turn to our major task, which is

to characterize the decadal-scale variations in the identified normal modes, if any, and to search for additional perturbations that may have escaped detection in previous analyses of the B ring edge.

For each mode, we scan a range of pattern speeds for the specified value of  $m$  in the neighborhood of the expected rate, as given by Eq. (2), in order to verify the reality of the mode and search for evidence of additional, nearby modes. Each scan is constructed in the same fashion: (i) the fit parameters for all  $m$ -values not being scanned are frozen at their best-fit values in Table 2; (ii) the fit parameters for the mode in question other than the pattern speed  $\Omega_p$  are allowed to float; (iii) the value of  $\Omega_p$  is varied across a range of  $\pm 1^\circ \text{ d}^{-1}$  centered on the predicted rate at the edge of the B ring, and (iv) for each assumed value of  $\Omega_p$  the remaining mode parameters  $A_m$  and  $\delta_m$  are adjusted to minimize the value of  $\chi^2$ . In this way, the significance of each mode can be assessed, with the parameters of all other modes kept constant at their optimal values.

The rms residuals far away from the best-fitting value of  $\Omega_p$  reflect the quality of the fit without the mode in question; for the dominant  $m = 2$  mode this is  $\sim 34 \text{ km}$ . For the weaker  $m = 3, 4$  and  $5$  modes, the baseline rms residuals are always under  $10 \text{ km}$ .

We begin with the dominant  $m = 2$  mode and then move on to the smaller-amplitude modes with  $m = 1, 3, 4$  and  $5$ .

### 6.1. Mimas and the dominant $m=2$ pattern

For the  $m = 2$  scan, both the forced and free amplitudes  $ae_0$  and  $ae_1$  were set to zero and the scanning program searched for a single, best-fitting mode. Fig. 3 shows the resulting scan. The predicted pattern speed for a free normal mode at the edge of the B ring is  $381.913^\circ \text{ d}^{-1}$ , as indicated by the vertical solid line, while the pattern speed for the forced Mimas 2:1 perturbation is at  $n_{\text{Mimas}} = 381.9835^\circ \text{ d}^{-1}$ , indicated by the dot-dashed line. As might be expected from the reference fit parameters in Table 2, the scan shows two distinct peaks in amplitude in the lower panel – and two corresponding minima in the post-fit residuals in the upper panel – at  $\sim 381.984^\circ \text{ d}^{-1}$  and  $382.075^\circ \text{ d}^{-1}$ . The higher and faster peak corresponds to the free  $m = 2$  mode while the lower and slower peak corresponds to the forced mode. The fitted libration frequency in Table 2 of  $\Omega_L = 0.1841^\circ \text{ d}^{-1}$  is twice the difference

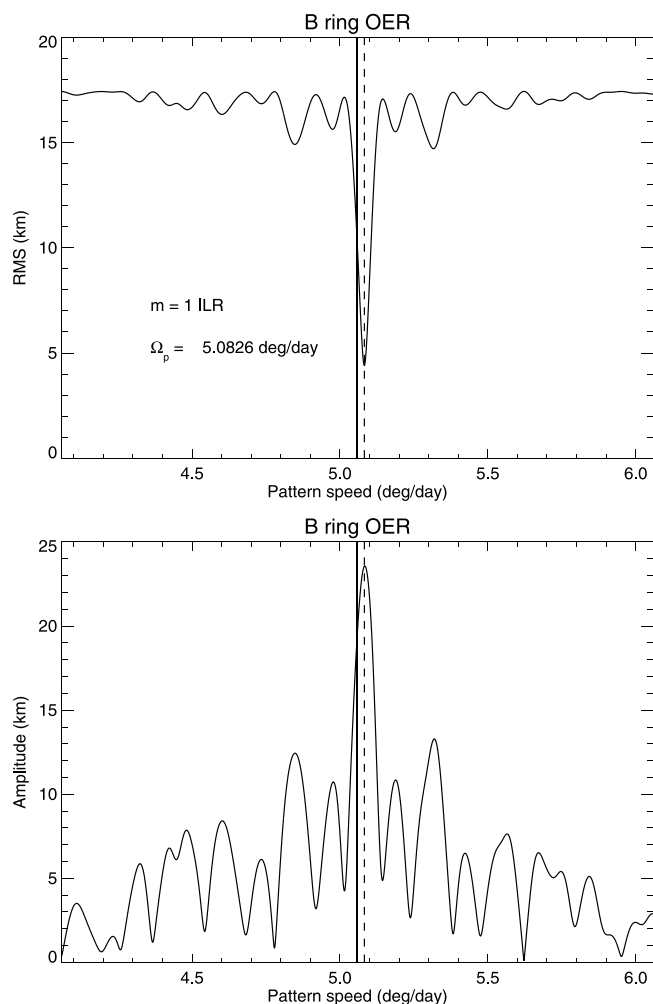


Fig. 7. A scan in pattern speed for  $m = 1$  normal modes, after removing the signatures of all other modes listed in Table 2. The format is the same as Fig. 3. Here significant power is seen at only one frequency, at  $5.083^\circ \text{ d}^{-1}$ , with a radial amplitude of 23.6 km and a minimum  $\sigma = 4.4$  km.

between the two mode peaks, as expected from Eq. (7). Note that, because the scanning procedure is only able to fit one pattern speed at a time, the minimum rms residual seen in Fig. 3 is still quite large at  $\sim 24$  km. Finally, we note that the resonance radius<sup>6</sup> corresponding to the free mode is located at  $\sim 117,537$  km, or 33 km interior to the mean radius of the B ring edge.

The existence of these two  $m = 2$  components of comparable strength results in a strong beat signature that can also be modeled as a circulation in the amplitude and phase of a single  $m = 2$  mode, with parameters as listed in Table 2. As a result, the amplitude of the  $m = 2$  pattern varies significantly during the *Cassini* mission, as first noted by Hedman et al. (2010) and Spitale and Porco (2010). This amplitude variation is clearly revealed in Fig. 4, which shows fits to subsets of the occultation data in eight different time intervals, selected to match the most densely-sampled periods. For each period, the radius residuals are calculated relative to our adopted reference model – except that the amplitudes of the  $m = 2$  terms,  $ae_0$  and  $ae_1$  are set to zero – and plotted vs the mode argument  $m\theta = m[\lambda - \Omega_p(t - t_0) - \delta_m]$  in Eq. (1), where in this case  $m = 2$  and  $\Omega_p = 381.9844^\circ \text{ d}^{-1}$ , corresponding to the mode forced by Mimas. In this figure, and in the similar ones to follow for other values of  $m$ , the upper left panel shows the complete set of *Cassini*

observations, while the eight successive panels reveal any systematic changes in both the amplitude and the phase of the  $m = 2$  pattern over time.

Because the argument  $m\theta$  includes the best-fitting global pattern speed and average phase for the mode, as represented by the parameters  $\Omega_p$  and  $\delta_m$  in Eq. (1), any shorter-term variations in the mode's phase will show up here as shifts in the position of the minimum in radius away from  $m\theta = 0$  from one time period to another. Indeed, such variations are clearly seen in this figure, with the radial minimum varying from  $m\theta = -86^\circ$  in 2006/07 to  $+120^\circ$  in 2017. Moreover, the amplitude varies from a minimum of  $\sim 6$  km in 2017 to a maximum of  $\sim 70$  km in 2009. To quantify these variations for the time period of the data shown in each panel, we fit a simple sinusoidal model to the distribution of radius residuals of the form:

$$dr = -ae \cos(m\theta - \phi_L), \quad (12)$$

following Eq. (3). The fitted values (and their formal uncertainties) for  $ae$  and  $\phi_L$  are listed in each panel.

These fitted variations in the amplitude of the  $m = 2$  mode are compared with those predicted by the circulating model in the reference fit in Fig. 5, where the colored symbols mark the times of the individual observations (blue for stellar occultations and red for RSS measurements). The eight large '+' symbols mark the fitted values for  $ae$  from Fig. 4, with the vertical component showing the formal uncertainty in the amplitude fit and the horizontal length spanning the time interval of the data used for the fit. The second and eighth intervals span the minima in  $A_2$  in 2006 and 2017, while the fourth interval spans the maximum in 2009. The observations sample a little over 2.5 libration cycles, or more than one rotation of the  $m = 2$  pattern relative to Mimas, albeit with several gaps owing to the absence of ring occultation measurements when *Cassini* was orbiting Saturn in the equatorial plane. Note that the amplitude lingers near its maximum value of 72.6 km for about a year, while moving rapidly through its minimum of 6.2 km in only a few months, making it difficult to catch the system in this state. In general, the agreement between the reference model and these individual fits over the eight separate time ranges is excellent. (Very similar results are obtained when the  $m = 2$  amplitude  $ae$  is computed using our adopted final fit.)

Because  $ae_1 > ae_0$  for the  $m = 2$  mode, there is a substantial variation in the phase of this mode compared to that predicted by Eq. (1). In fact, our model implies that  $\phi_L$  actually circulates through  $360^\circ$ , as concluded originally by Spitale and Porco (2010), although the system spends relatively little time with  $|\phi_L| > 90^\circ$ . This may be seen in Fig. 6, which shows the distribution of the B ring edge measurements used in this study along with the corresponding phases predicted by the reference model  $\phi_L$ . We find that  $|\phi_L| > 90^\circ$  for about 9 months every 5.4 years, centered on the times of the amplitude minima in 2006.7, 2012.1 and 2017.5. (Amplitude maxima occur in 2009.4 and 2014.8, when  $\phi_L$  passes through zero.)

Updated values for the  $m = 2$  libration parameters are included in our final fit that includes all known modes and librations (see Table 3 below). Following a similar process to that used for the other wavenumbers (described below), we also scanned the residuals to this final fit to search for any additional, previously-undetected contributions to the  $m = 2$  pattern, but found none.

## 6.2. The $m=1$ pattern

Fig. 7 shows the pattern speed scan for the  $m = 1$  mode, whose predicted value at the edge of the B ring is  $\dot{\omega}_{\text{sec}} = 5.059^\circ \text{ d}^{-1}$ , as indicated by the vertical solid line. Here we see a single strong peak in amplitude at  $\Omega_p = 5.083^\circ \text{ d}^{-1}$ , somewhat faster than the predicted value. The corresponding resonance radius is  $\sim 117,419$  km, or 151 km interior to the mean radius of the ring edge.

The reference fit for the  $m = 1$  mode assumes a constant amplitude over the entire set of observations, but Nicholson et al. (2014a) noted

<sup>6</sup> That is, the semimajor axis at which Eq. (2) is satisfied.

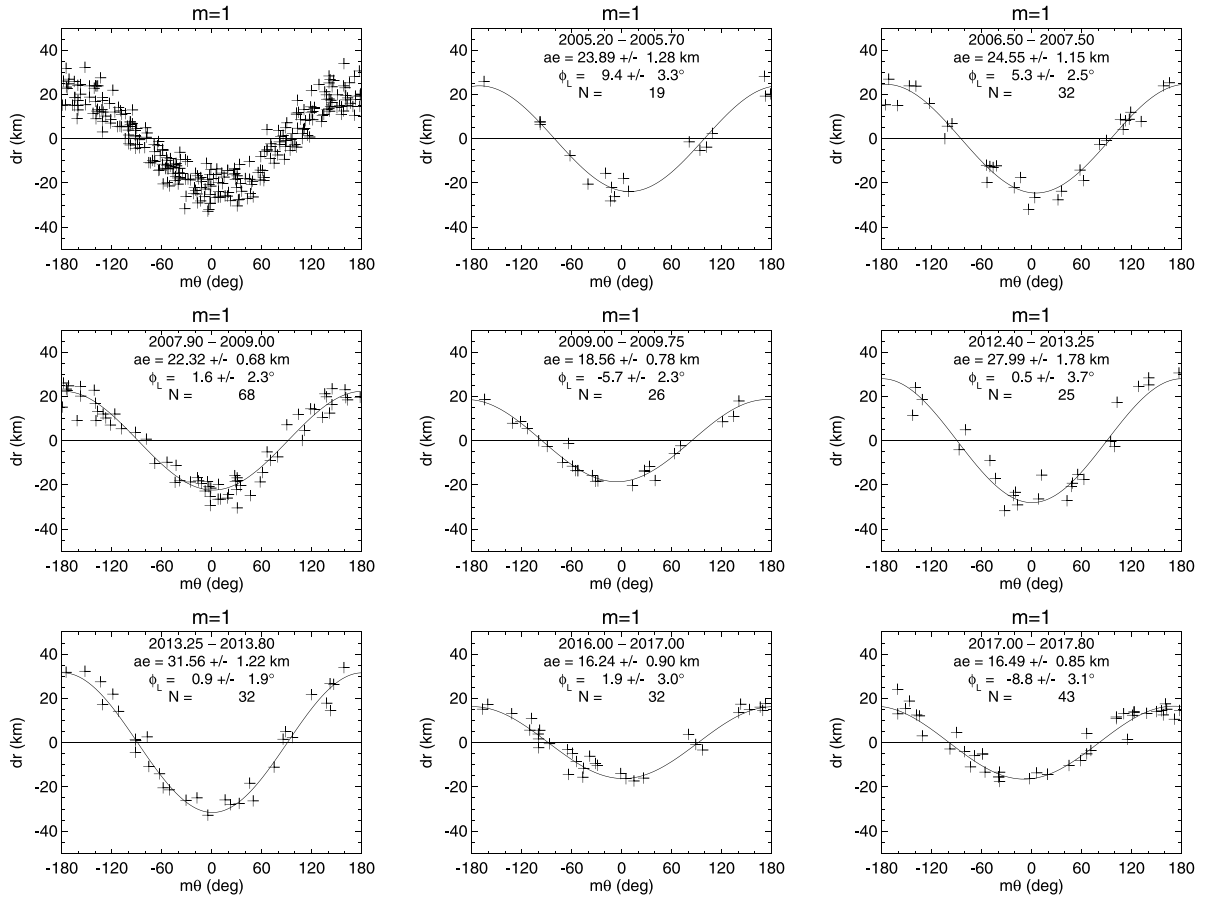


**Fig. 8.** Radius residuals from our final B ring model when the  $m = 1$  terms are set to zero, plotted as a function of  $m\theta$ , for  $\Omega_p = 5.0824^\circ \text{ d}^{-1}$ . The upper left panel shows the full set of observations, with substantial scatter. The observations are divided into eight different time intervals in the remaining panels, as in Fig. 4, showing substantial systematic variations in the amplitude of the  $m = 1$  pattern over time, particularly after 2010. See text for details of the model fit results included in these panels.

that  $A_1$  decreased slightly from  $\sim 25$  km in 2005 to  $\sim 20$  km in 2008/09 (see their Fig. 4). By separating the observations into the same eight time intervals as for the  $m = 2$  mode, we see a more complete picture of the time variability of the  $m = 1$  mode in Fig. 8. (In this and in subsequent similar figures, we compute the residuals relative to our final adopted model for the B ring, rather than to the reference model, since this more realistically shows the radial variations that contribute to the final fit for each wavenumber.) With a doubling of the timespan of the observations, we confirm the results of Nicholson et al. (2014a) but find that  $A_1$  subsequently increased to  $\sim 30$  km in 2013, before falling back to  $\sim 17$  km in 2016/17.

Given this evidence for time variability in the  $m = 1$  amplitude, we repeated our frequency scan of the B ring edge residuals after removal of the main  $m = 1$  signal, as well as all other detected normal modes from our final fit (see Table 3 below), with the results shown in Fig. 9. We find a much weaker but statistically significant signal with  $\Omega_p = 5.206^\circ \text{ d}^{-1}$  and an amplitude of 4.4 km. Combined with the original  $m = 1$  mode with  $\Omega_p = 5.0824^\circ \text{ d}^{-1}$ , this suggests a libration with  $\Omega_L \simeq 0.123^\circ \text{ d}^{-1}$ , corresponding to a period of  $\sim 8.0$  yr.

Although including this libration term in the  $m = 1$  mode does modestly improve the overall fit, it fails to capture well the amplitude variations seen in Fig. 8. A subsequent frequency scan, after inclusion of the above libration term, shows evidence for a third statistically-significant  $m = 1$  component with  $\Omega_p = 5.250^\circ \text{ d}^{-1}$  and an amplitude of  $\sim 2.8$  km, as shown in Fig. 10. This suggests a second libration term with  $\Omega_L \simeq 0.167^\circ \text{ d}^{-1}$ , corresponding to a period of  $\sim 5.9$  yr.

Once this additional component is included in the orbit fit, the calculated amplitude and phase variations of the  $m = 1$  mode provide a significantly better match to the observations, as shown in Fig. 11. We

caution the reader, however, that while this multi-component model may match our observations over their 13 yr time interval, we do not know if these librations will maintain their amplitudes, periods, and phases over timescales of centuries. Instead, it might be better to think of them simply as quantifying the variability of the  $m = 1$  shape of the B ring edge over the limited period of *Cassini* observations.

Table 3 includes the final values for all three  $m = 1$  components in our adopted fit, with amplitudes of  $ae_0 = 23.56 \pm 0.51$  km,  $ae_1 = 4.42 \pm 0.63$  km, and  $ae_2 = 2.84 \pm 0.53$  km. The final libration frequencies are  $\Omega_{L,1} = 0.1145 \pm 0.0096^\circ \text{ d}^{-1}$  and  $\Omega_{L,2} = 0.1671 \pm 0.0150^\circ \text{ d}^{-1}$ .

### 6.3. The $m=3$ pattern

Fig. 12 shows the scan for the  $m = 3$  mode, whose predicted pattern speed at the edge of the B ring is  $\Omega_p = 507.530^\circ \text{ d}^{-1}$ . Here we see a single strong peak in amplitude at  $\Omega_p = 507.7189^\circ \text{ d}^{-1}$ , again faster than the predicted value, but also two secondary peaks at slightly lower frequencies. The resonance radius corresponding to the strongest peak is  $\sim 117,541$  km, or 29 km interior to the mean radius of the ring edge.

As for the  $m = 1$  mode, we again find substantial long-term variations in the amplitude and phase over time, as shown in Fig. 13, which follows the same format as Figs. 4 and 8. Beginning at  $\sim 20$  km in 2005,  $ae$  fell steadily to a minimum of  $\sim 7$  km in 2009–2013, rose to 11 km in 2016, before falling slightly in 2017. The steady decline between 2005 and 2009 was also noted by Nicholson et al. (2014a).

In our initial attempt to match this pattern, we included a single libration term for  $m = 3$ , treating the libration frequency  $\Omega_L$ , amplitude  $ae_1$ , and phase  $\delta_L$  as free parameters. The results matched the overall trend in the amplitude of the mode, but with physically implausible

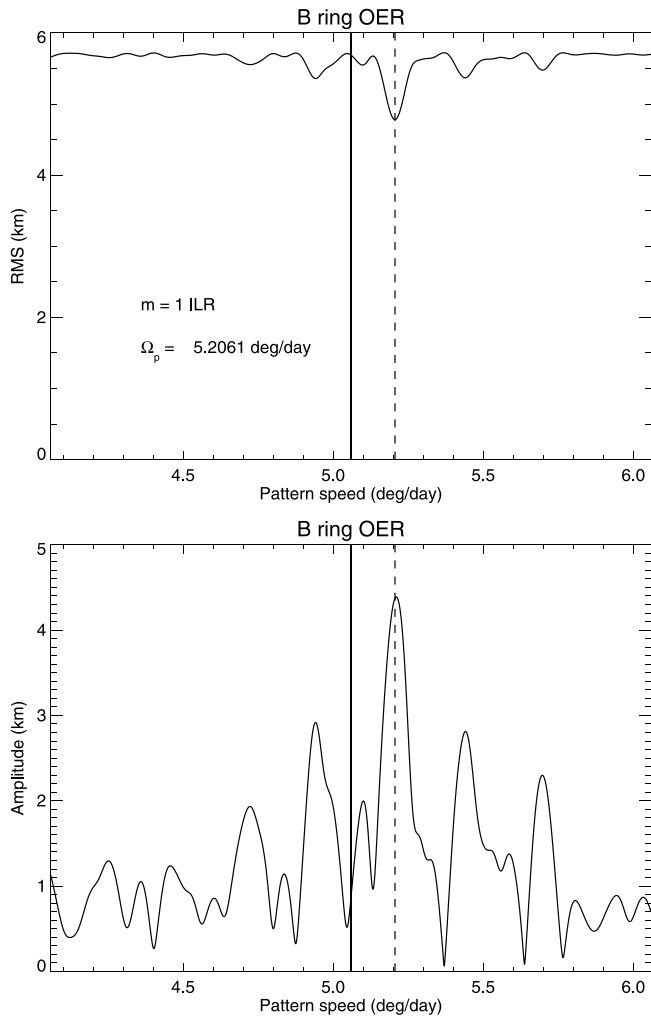


Fig. 9. The signature of a second  $m = 1$  component with  $\Omega_p = 5.206^\circ \text{ d}^{-1}$  and an amplitude of  $\sim 4.4$  km, as seen in a normal mode scan. The primary component is at  $\Omega_p = 5.083^\circ \text{ d}^{-1}$ , as shown in Fig. 7, while the predicted pattern speed at the edge of the B ring is  $5.059^\circ \text{ d}^{-1}$ .

values for  $ae_0$  and  $ae_1$  of hundreds of km and a libration period of hundreds of years, much longer than those found for the  $m = 1$  and  $m = 2$  modes. The two components nearly cancel each other out during the comparatively short interval of the *Cassini* observations, but lead to much larger – and implausible – predicted variations at earlier and later times.

As with the  $m = 1$  case, we then fitted for a second libration component with much more satisfactory results, as shown in Fig. 14. The dominant component, however, has an uncomfortably long period of almost 20 yrs – longer than the 13 yr span of the *Cassini* observations – that is not well-determined by the fit. Table 3 includes the final values for all three  $m = 3$  components in our adopted fit, with amplitudes of  $ae_0 = 11.19 \pm 0.53$  km,  $ae_1 = 7.41 \pm 0.64$  km, and  $ae_2 = 2.15 \pm 0.49$  km. The final libration frequencies are the poorly-constrained value of  $\Omega_{L,1} = -0.050^\circ \text{ d}^{-1}$  and  $\Omega_{L,2} = 0.1342 \pm 0.0086^\circ \text{ d}^{-1}$ . (Note that a negative value of  $\Omega_L$  implies that the eccentricity vector rotates in a clockwise direction in  $[h, k]$  space and that, if the libration is interpreted in terms of the beating of two modes with the same  $m$ , that  $\Omega_1 < \Omega_0$  in Eq. (7)).

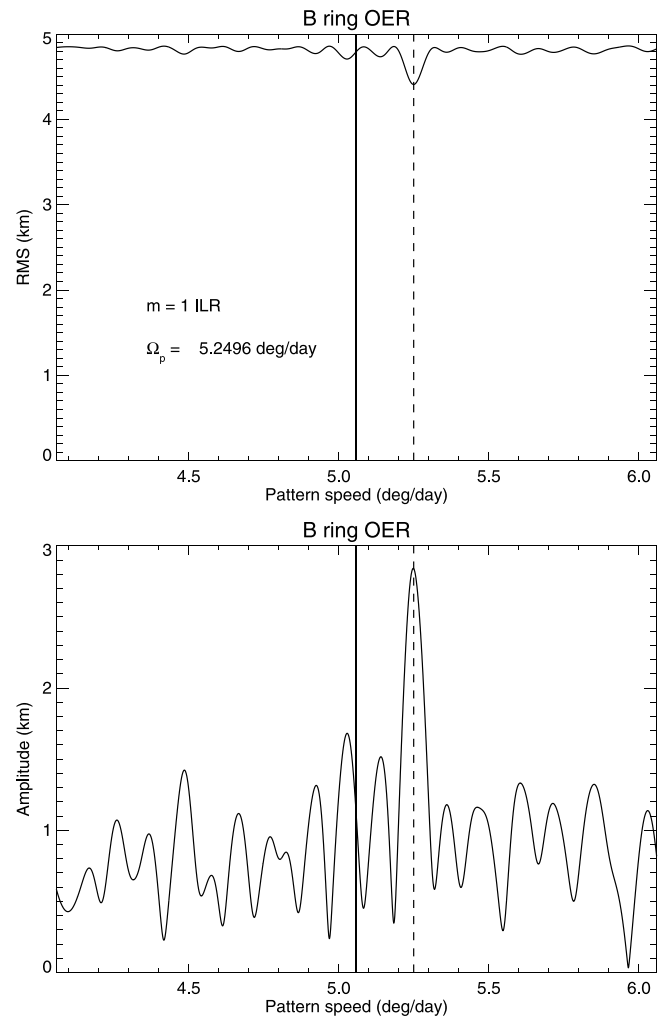


Fig. 10. The signature of a third  $m = 1$  component with  $\Omega_p = 5.250^\circ \text{ d}^{-1}$  and amplitude  $\sim 2.8$  km. The primary and secondary components are at  $\Omega_p = 5.083^\circ \text{ d}^{-1}$  and  $5.206^\circ \text{ d}^{-1}$ , as shown in Figs. 7 and 9.

#### 6.4. The $m=4$ pattern

Fig. 15 shows the scan for the  $m = 4$  mode, for which the predicted pattern speed at the edge of the B ring is  $\Omega_p = 570.339^\circ \text{ d}^{-1}$ . Again we see a single strong peak in amplitude at a pattern speed slightly faster than the predicted value, or  $\Omega_p = 570.529^\circ \text{ d}^{-1}$ . The corresponding resonance radius is  $\sim 117,544$  km, or 26 km interior to the mean radius of the ring edge.

The observed variations in the  $m = 4$  contribution to the shape of the B ring edge over time are shown in Fig. 16, in the same format as Figs. 4, 8 and 13. As is the case for  $m = 1$  and  $m = 3$ , we see substantial changes in amplitude over the course of the observations. Although the average amplitude is  $\sim 8$  km over the period 2005–2017 (see Table 2), it reached a minimum of  $\sim 2.9$  km in 2009 and a maximum of  $\sim 14$  km in 2017, without any clear periodicity.

A libration frequency scan suggested a dominant frequency  $\Omega_L \approx 0.17^\circ \text{ d}^{-1}$ , corresponding to a period of  $\sim 5.8$  yr, with an amplitude of  $\sim 3$  km, but a fit with such a single term was again rather unsatisfactory. A subsequent frequency scan of the radius residuals after inclusion of the single libration revealed a statistically significant additional component. A greatly improved fit to the observed amplitudes and phases was obtained with the resulting two-term libration model, as shown in Fig. 17. Table 3 includes the final values for all three  $m = 4$  components in our adopted fit, with amplitudes of  $ae_0 = 7.32 \pm 0.47$

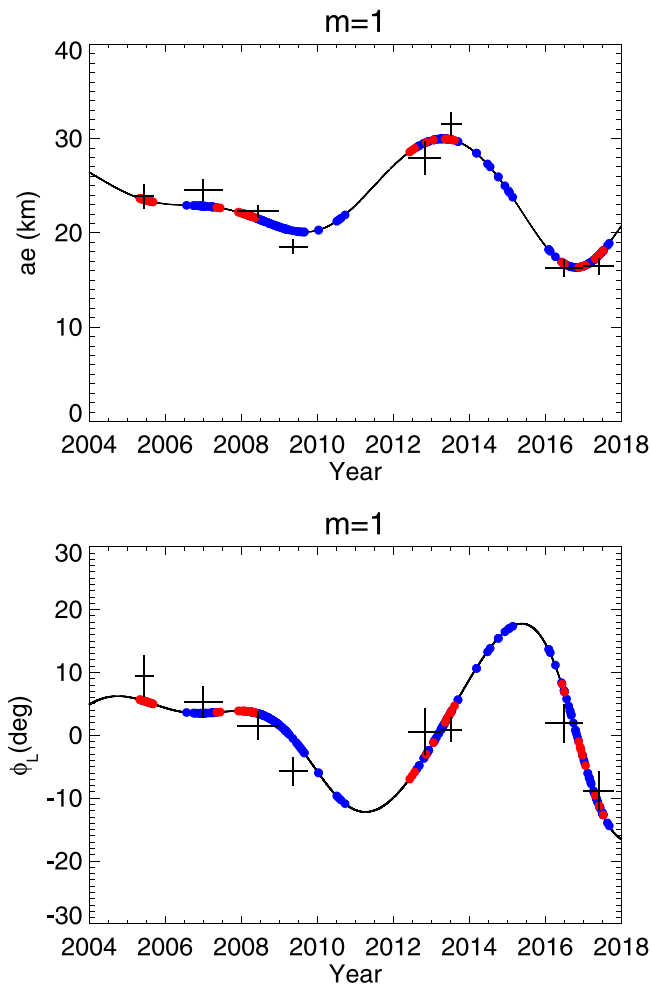


Fig. 11. Variation in the amplitude  $A_1$  and phase  $\phi_L$  of the  $m = 1$  mode over time incorporating two libration terms with periods of 8.0 and 5.9 yr and amplitudes of 4.4 and 2.8 km, respectively. The model curves match the fitted values for the mode amplitude and libration phase obtained from fits to selected time intervals shown in Fig. 8 over the full span of the observations, although extending these periodic terms into the unobserved past or future is probably unwarranted.

km,  $ae_1 = 2.79 \pm 0.47$  km, and  $ae_2 = 2.56 \pm 0.45$  km. The final libration frequencies are  $\Omega_{L,1} = -0.2032 \pm 0.0092^\circ \text{ d}^{-1}$  and  $\Omega_{L,2} = 0.1676 \pm 0.0095^\circ \text{ d}^{-1}$ .

### 6.5. The $m=5$ pattern

Finally we have Fig. 18, which shows the scan for the  $m = 5$  mode, whose predicted pattern speed at the edge of the B ring is  $\Omega_p = 608.025^\circ \text{ d}^{-1}$ . Again we see a single strong peak in amplitude at  $\Omega_p = 608.206^\circ \text{ d}^{-1}$ , slightly faster than the predicted value. The corresponding resonance radius is  $\sim 117,547$  km, or 23 km interior to the mean radius of the ring edge. This is a relatively weak mode, with an average amplitude of about 6 km, but varying between about 4 and 8 km, as shown in Fig. 19. There appear to be at least three amplitude minima within the period of Cassini observations, in 2005, 2008 and 2016/17, suggesting a fairly short libration period.

A libration frequency scan revealed a single best-fitting value of  $\Omega_L \simeq 0.44^\circ \text{ d}^{-1}$ , corresponding to a period of 2.25 yr, a result that was borne out by a least-squares fit with a single libration term. Fig. 20 shows the resulting model amplitude and phase variations over time. Although the relatively rapid libration is less well-sampled by the eight snapshots in Fig. 19 than one would like, the model does fit the observations reasonably well. Our final model in Table 3 has  $m = 5$

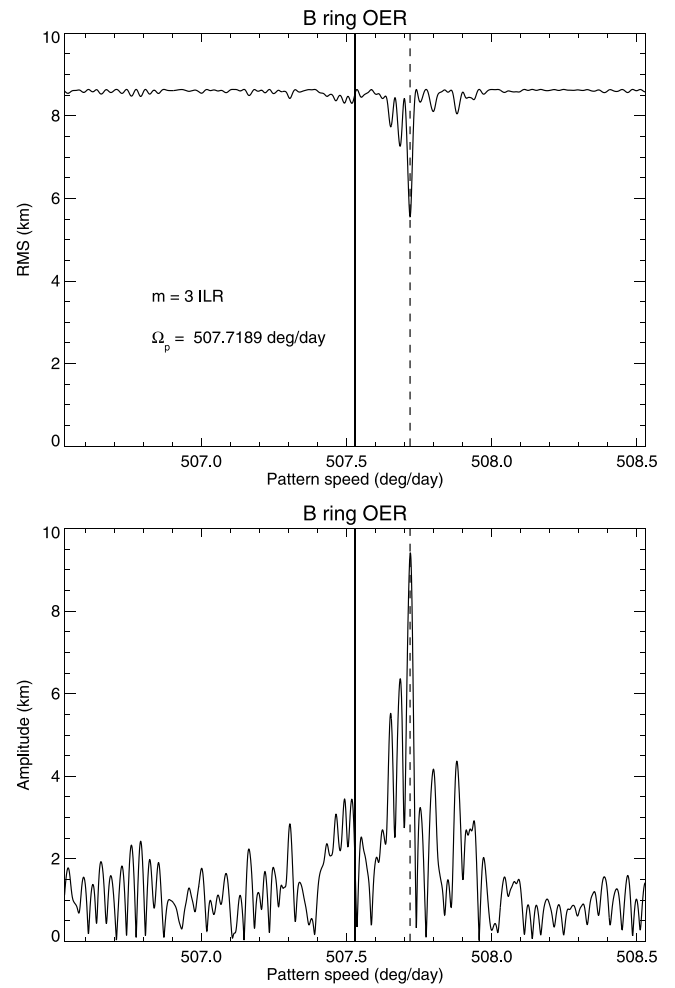


Fig. 12. A scan in pattern speed for  $m = 3$  normal modes, after removing the signatures of all other modes listed in Table 2. The format is the same as Fig. 3. Here the maximum power is seen at one frequency, at  $507.7189^\circ \text{ d}^{-1}$ , with a radial amplitude of 9.5 km and a minimum  $\sigma = 5.6$  km, but there are two substantial secondary peaks at slightly lower frequencies.

amplitudes of  $ae_0 = 5.42 \pm 0.44$  km and  $ae_1 = 1.55 \pm 0.44$  km, with a libration frequency  $\Omega_L = 0.4353 \pm 0.0116^\circ \text{ d}^{-1}$ .

### 6.6. Summary of libration models

Table 3 summarizes all the parameters for our final multi-mode fit to the B ring edge, including the libration terms. For each value of  $m$  we list the basic mode parameters  $ae_0$ ,  $\Omega_p$  and  $\delta_m$ , and for each libration we list  $ae_j$ ,  $\Omega_{L,j}$  and  $\delta_{L,j}$ , as well as the libration period  $P_{L,j}$ . (Recall that for librating modes the overall amplitude  $A_m = ae$  is not constant, but given by Eqs. (4) and (5) or (8).)

The rms residual per degree of freedom of the fit is 4.7 km, a significant improvement over the 7.0 km in the reference fit in Table 2 and the 7.8 km achieved by Fit 11 of Nicholson et al. (2014a). This improvement primarily reflects the addition of libration terms for the modes with  $m = 1, 3, 4$  and 5. Fig. 21 shows a histogram of the post-fit residuals in radius, compared to a Gaussian distribution with a standard deviation of 4.7 km. The 11 points with residuals  $>20$  km (i.e.,  $>4\sigma$ ) are listed in Table 1 and were excluded from the fit.

Compared with the reference fit, which uses the same data set, the amplitude, phase and pattern speed of the forced mode due to the Mimas 2:1 ILR are all unchanged, within their stated uncertainties. Our final fit has slightly smaller primary amplitudes for the free  $m = 2, 4$  and

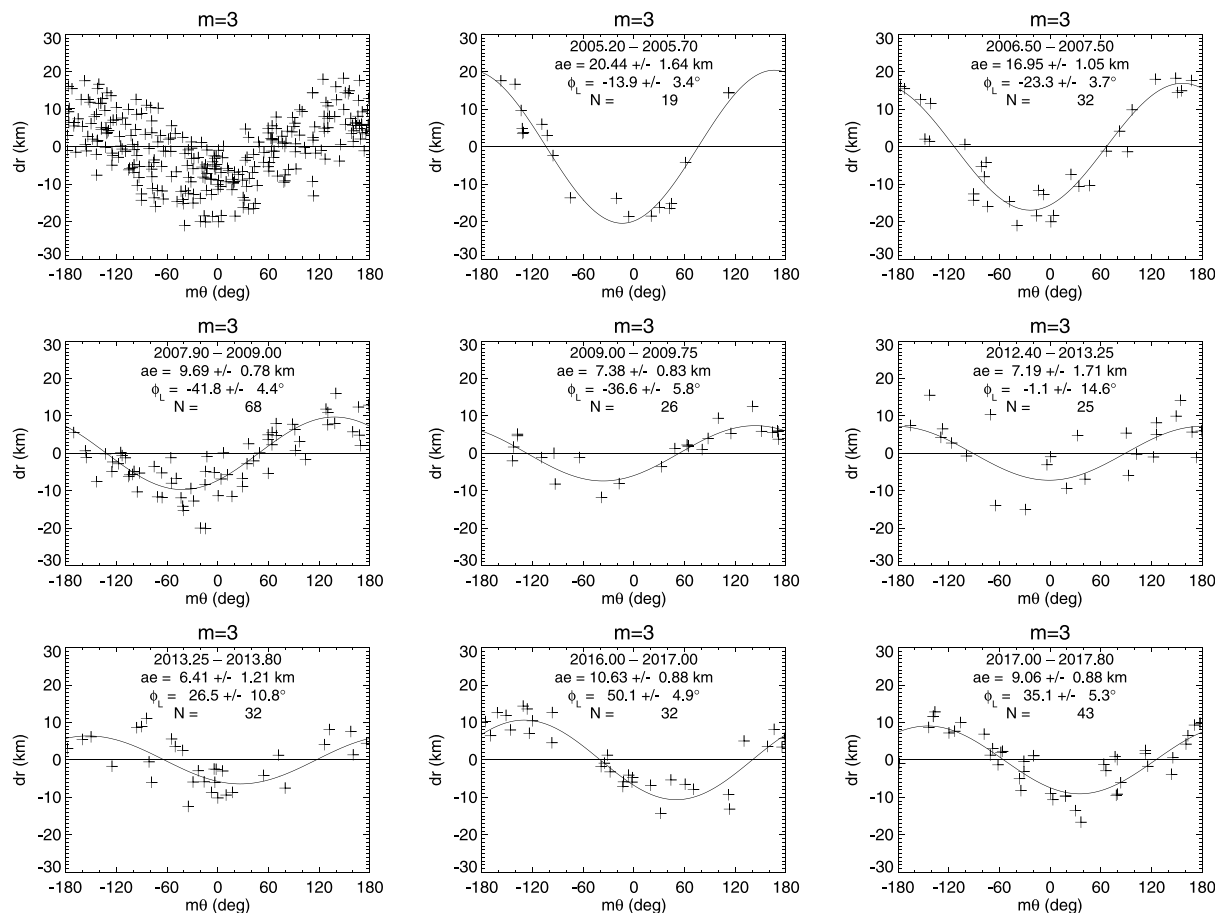


**Fig. 13.** Radius residuals from our final B ring model when the  $m = 3$  terms are set to zero, plotted as a function of  $m\theta$ , where  $\Omega_p = 507.71325^\circ \text{ d}^{-1}$ . The upper left panel shows the full set of observations, with their substantial scatter. The observations are divided into eight different time intervals in the remaining panels, which show substantial systematic variations in the amplitude and phase of the  $m = 3$  pattern over time. The amplitude decreased sharply between 2005 and 2010, remained fairly constant through 2013 and rose again in 2016 and 2017, though remaining well below the level of the earliest observations. See text for details of the model fit results included in these panels.

5 modes, and slightly larger amplitudes for the  $m = 1$  and  $m = 3$  modes. The pattern speeds of the free modes are also statistically unchanged, with the exception of the  $m = 3$  mode for which  $\Omega_p$  has decreased by  $0.0052 \pm 0.0008^\circ \text{ d}^{-1}$ .

Libration periods range from 2.25 yr for the  $m = 5$  mode to  $\sim 20$  yr for the  $m = 3$  mode, but most are in the range of 5–9 yrs. Two of the fitted libration frequencies are negative, meaning that the corresponding eccentricity vectors rotate clockwise in the  $[h, k]$  plane, opposite to the direction of  $\Omega_p$ , and that as a result  $\Omega_1 < \Omega_0$ .

Fig. 22 shows the mode amplitudes ( $ae_0$  and  $ae_j$ ), grouped by the value of  $m$ . For  $m = 2$ , the free eccentricity is larger than the forced, implying that the overall  $m = 2$  pattern circulates, rather than librates, with respect to the mean longitude of Mimas. With the exception of the  $m = 2$  mode, the primary mode amplitudes range from 24 to 5 km while the libration amplitudes lie in the range 2–7 km. Although the primary mode amplitudes generally decrease with increasing  $m$ , the latter show no obvious pattern.

Finally, we remind the reader that the relatively long libration periods – in some cases comparable to, or even longer than, the time span of the *Cassini* data – argue for caution in their interpretation. In particular, it is unclear whether the amplitude variations in the modes are truly periodic, or are instead more irregular in nature.

## 7. Discussion

### 7.1. The resonant cavity model and B ring surface mass densities

The most surprising result to emerge from the present study is the apparent libration exhibited by all of the normal modes identified at

the outer edge of the B ring, as summarized in Table 3 and Fig. 22. As discussed briefly in Section 2, our model for a librating streamline admits at least two distinct dynamical interpretations: one in which a single mode oscillates in amplitude and phase, and the other in which two or more stable modes with the same value of  $m$  and similar pattern speeds interfere to produce a beating pattern. (A third possible interpretation is that this is the outcome of nonlinear and non-resonant coupling between multiple modes with different values of  $m$ , and will be briefly discussed at the end of this section.) An example of the first case is a normal mode whose amplitude and phase vary due to a viscous overstability, as originally envisioned by Borderies et al. (1985). In the second case, a ring might support two or more independent edge modes with the same  $m$  but different numbers of radial nodes  $n_r$ , and thus slightly different pattern speeds (Longaretti, 2018). These very similar modes can then beat against one another to produce the appearance of a single mode with a variable amplitude.

As we noted in Section 2, these two situations are indistinguishable when only the shape of a single ring streamline – such as a ring edge – is known, without any information on the radial variation in ring eccentricity. But it might be possible, at least in principle, to use radial optical depth or brightness profiles interior to the ring edge to sort out which of these alternative hypotheses better fits the actual rings, perhaps by identifying radial nodes due to beating between multiple modes. In fact, this region was examined briefly by Hedman and Nicholson (2019) in their study of axisymmetric features in the rings, who found that while the overall structure within  $\sim 500$  km of the B ring edge seems to be dominated by perturbations with  $m = 1$  – presumably due to the edge mode studied in the present paper – there is

**Table 3**  
Multi-mode fit to Cassini data.

Parameter	Symbol	Value
mean radius	$a(\text{km})$	$117570.48 \pm 0.29$
Epoch		UTC 2008 Jan 1 12:00
RMS residual	$\sigma(\text{km})$	4.71
# data	N	294
Fit ID		Sa025S-Bring-final_20220111a

Symbol	1	2	$m$ 3	4	5
$ae$ (km)	$23.56 \pm 0.51$	$33.61 \pm 0.45$	$11.19 \pm 0.53$	$7.32 \pm 0.47$	$5.42 \pm 0.44$
$\Omega_p$ ( $^\circ \text{d}^{-1}$ )	$5.0824 \pm 0.0012$	$381.98441 \pm 0.00031$	$507.71325 \pm 0.00070$	$570.52829 \pm 0.00084$	$608.20674 \pm 0.00065$
$\delta$ ( $^\circ$ )	$64.21 \pm 1.87$	$165.99 \pm 0.51$	$31.00 \pm 1.01$	$9.62 \pm 1.34$	$68.20 \pm 1.28$
$\Delta a_{res}$ (km)	$-151.03 \pm 7.74$	$-14.70 \pm 0.06$	$-28.14 \pm 0.11$	$-25.93 \pm 0.11$	$-23.47 \pm 0.08$
$ae_1$ (km)	$4.42 \pm 0.63$	$37.59 \pm 0.46$	$7.41 \pm 0.64$	$2.79 \pm 0.47$	$1.55 \pm 0.44$
$\Omega_{L,1}$ ( $^\circ \text{d}^{-1}$ )	$0.1145 \pm 0.0096$	$0.1838 \pm 0.0006$	[ -0.05 ]	$-0.2032 \pm 0.0092$	$0.4353 \pm 0.0116$
$P_{L,1}$ (yr)	$8.609 \pm 0.718$	$5.362 \pm 0.017$	[ 19.713 ]	$4.851 \pm -0.219$	$2.264 \pm 0.060$
$\delta_{L,1}$ ( $^\circ$ )	$193.60 \pm 22.47$	$96.11 \pm 1.37$	$90.97 \pm 3.66$	$57.75 \pm 14.00$	$161.40 \pm 23.41$
$ae_2$ (km)	$2.84 \pm 0.53$		$2.15 \pm 0.49$	$2.56 \pm 0.45$	
$\Omega_{L,2}$ ( $^\circ \text{d}^{-1}$ )	$0.1671 \pm 0.0150$		$0.1342 \pm 0.0086$	$0.1676 \pm 0.0095$	
$P_{L,2}$ (yr)	$5.900 \pm 0.529$		$7.347 \pm 0.470$	$5.881 \pm 0.332$	
$\delta_{L,2}$ ( $^\circ$ )	$350.70 \pm 34.50$		$247.25 \pm 17.50$	$217.29 \pm 13.08$	

Note: Subscripts 1 or 2 indicate libration terms. Values in square brackets [...] were held fixed.

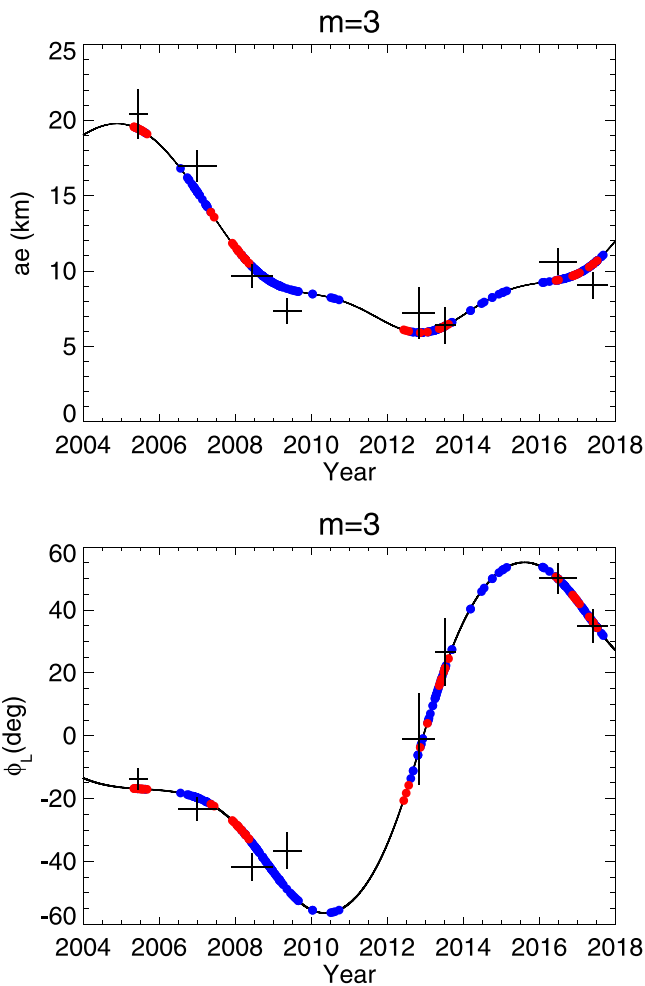


Fig. 14. Variation in the amplitude  $A_3$  and phase  $\phi_L$  of the  $m = 3$  mode over time incorporating two libration terms with periods of 19.7 and 7.3 yr and amplitudes of 7.4 and 2.2 km, respectively. The model curves match the fitted values for the mode amplitude and libration phase obtained from fits to selected time intervals shown in Fig. 13 over the full span of the observations, although the unusually long period of the first libration is not tightly constrained by the observations.

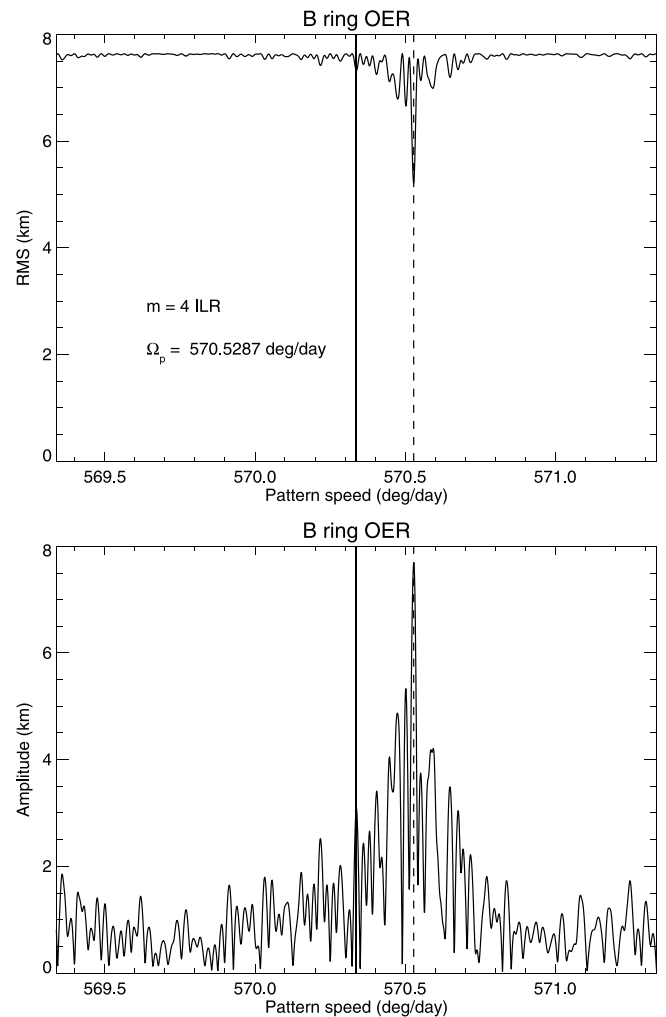


Fig. 15. A scan in pattern speed for  $m = 4$  normal modes, after removing the signatures of all other modes listed in Table 2. The format is the same as Fig. 3. Here the maximum power is seen at one frequency, at  $570.529^\circ \text{d}^{-1}$ , with a radial amplitude of 7.7 km and a minimum  $\sigma = 5.2$  km.

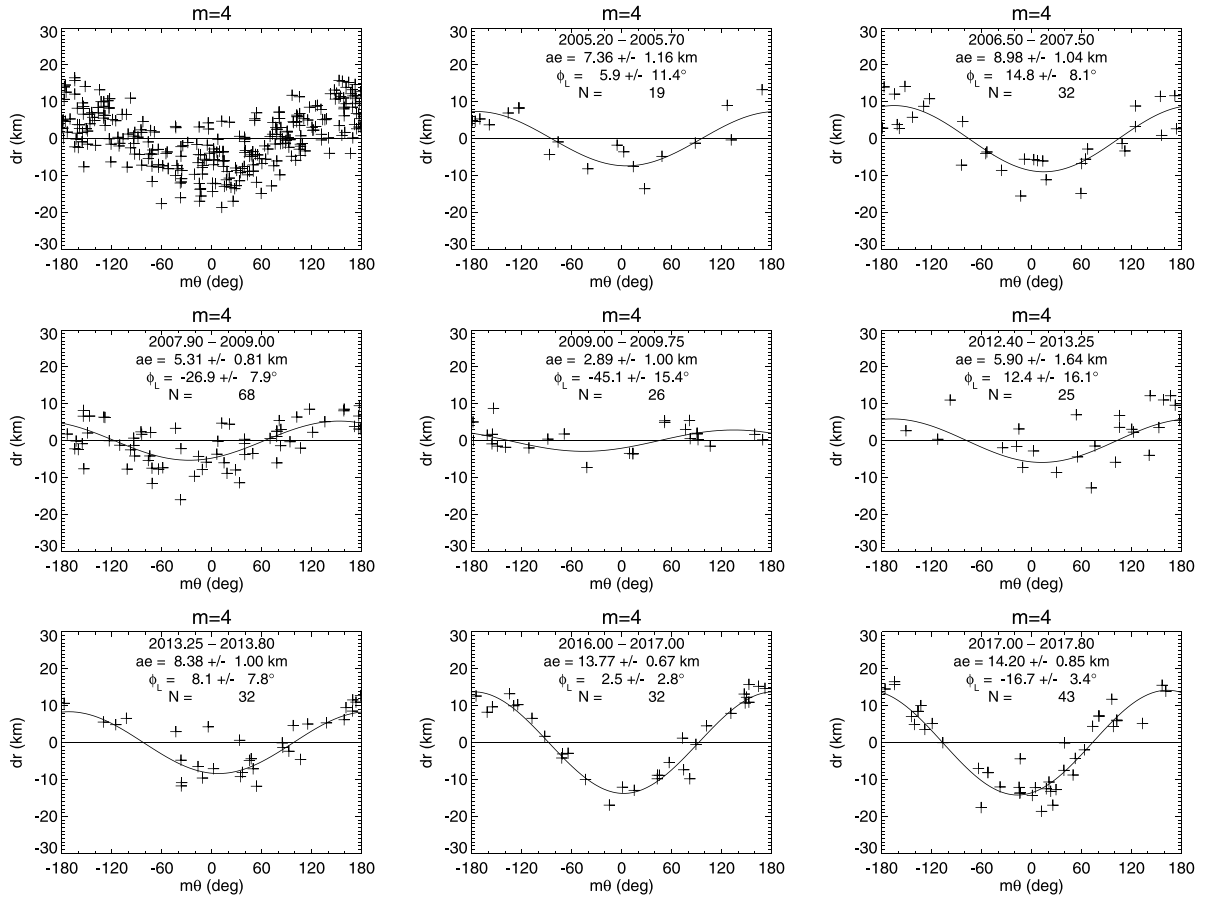


Fig. 16. Radius residuals from our final B ring model when the  $m = 4$  terms are set to zero, plotted as a function of  $m\theta$ , where  $\Omega_p = 570.52829^\circ \text{ d}^{-1}$ . The upper left panel shows the full set of observations, with their scatter. The observations are divided into eight different time intervals in the remaining panels, which show substantial variations in the amplitude and phase of the  $m = 4$  pattern over time, with the amplitude decreasing to below 3 km in 2009 and then rising to above 14 km in 2017. See text for details of the model fit results included in these panels.

also evidence in some imaging mosaics for a density wave with  $m = 0$  propagating inwards from the ring edge, at least in the radial range 177,220–117,400 km. However, the complexity and time-variability of this region, combined with the large-amplitude radial perturbations within  $\sim 100$  km of the ring edge due to the librating  $m = 2$  mode, have so far defeated efforts at unraveling all of these superimposed structures. It is likely that a full analysis will require simultaneous modeling of the *Cassini* imaging and occultation data, something that is beyond the scope of the current work.

So in the spirit of hypothesis testing, and because it is the more susceptible to the simple kinematic modeling adopted in Section 2, we will assume here that the second, multi-mode interpretation is correct. According to the edge-mode model, as outlined by Spitale and Porco (2010) and French et al. (2016) and reviewed by Nicholson et al. (2018), a normal mode at the edge of a ring with a specified pattern speed  $\Omega_p$  can be viewed as a pair of free density waves trapped in a resonant cavity between the radius of the corresponding Lindblad resonance  $a_{\text{res}}$  (where Eq. (2) is satisfied) and the edge of the ring. For an outer ring edge, an  $m$ -armed trailing spiral density wave is generated at the ILR, propagates outwards until it encounters the outer edge of the ring (or the inner edge of a gap), and then reflects as an inward-propagating leading wave. This wave then reflects at the ILR to produce an outward-propagating trailing wave, thus completing the cycle. The angular frequency of the wave  $\omega = m\Omega_p$  is determined indirectly via the density wave dispersion relation  $\omega(k)$  and the requirement that the total change in phase around each cycle of the cavity is zero or a multiple of  $2\pi$ .

Under the assumption that each of the libration terms we have identified above is in fact due to beating between a primary normal

mode, with pattern speed  $\Omega_p$ , and a secondary mode with pattern speed  $\Omega_{p,j}$ , then from Eq. (7) above we have

$$\Omega_{p,j} = \Omega_p + \Omega_{L,j}/m, \quad (13)$$

where  $\Omega_{L,j}$  is the fitted libration frequency. (The subscript  $j$  allows for the possibility of more than one libration term for a particular value of  $m$ , each of which represents a new pattern speed  $\Omega_{p,j}$ .) Note that if  $\Omega_{L,j} < 0$ , then  $\Omega_{p,j} < \Omega_p$  and the resonant radius of the secondary mode is external to that corresponding to  $\Omega_p$ . We can then calculate the resonance radii  $a_{\text{res}}$  of these putative secondary modes from their pattern speeds via Eq. (2), as usual, and thus their distances  $\Delta a_{\text{res}}$  from the edge of the B ring, assumed to be at 117,570.48 km. The results of this calculation, based on the libration frequencies given in Table 3, are plotted in Fig. 23.

Given  $\Delta a_{\text{res}}$ , the average surface mass density in the resonant cavity  $\Sigma$  can be estimated using the WKB expression for the wavelength of density waves in the vicinity of a Lindblad resonance, leading to the approximate expression (see Section 6.3 of Nicholson et al., 2014a):

$$\Sigma = \left[ 3(m-1) + \frac{21}{2} J_2 (R/a_{\text{res}})^2 \right] \frac{M_p \Delta a_{\text{res}}^2}{8\pi^2 \Gamma a_{\text{res}}^4}, \quad (14)$$

where  $M_p$ ,  $R$  and  $J_2$  are the mass, equatorial radius and second zonal gravity harmonic of Saturn. Note that, for a given surface mass density  $\Sigma$ ,  $\Delta a_{\text{res}}$  decreases monotonically for larger values of  $m$  but increases for larger values of  $n_r$ .

The numerical factor  $\Gamma$  specifies the number of density wavelengths between the resonant radius and the edge of the ring, where the wave

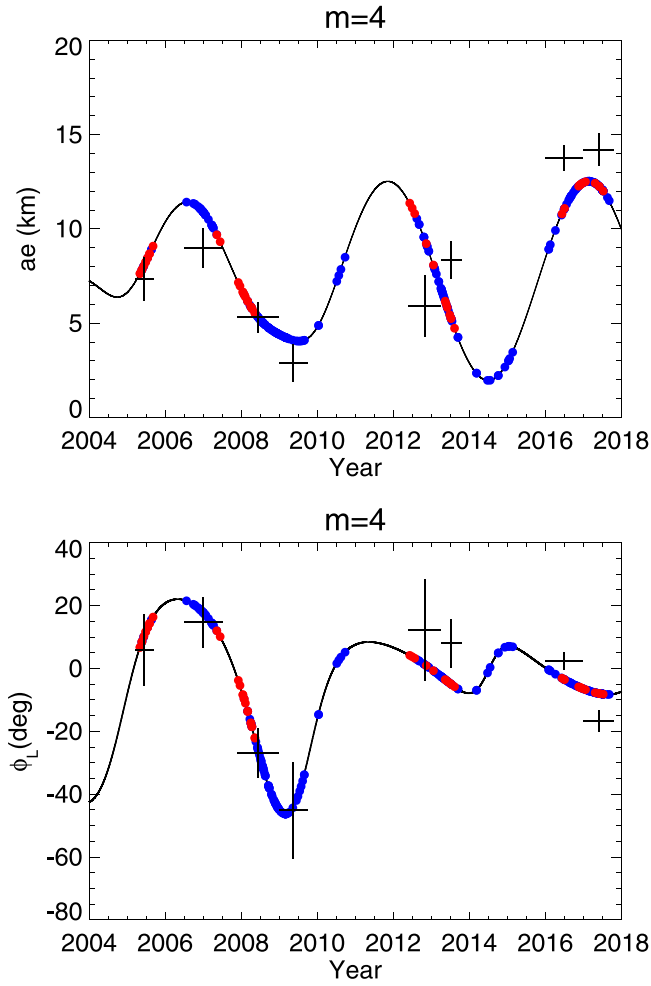


Fig. 17. Variation in the amplitude  $A_4$  and phase  $\phi_L$  of the  $m = 4$  mode over time incorporating two libration terms with periods of 4.9 and 5.9 yr and amplitudes of 2.8 and 2.6 km, respectively. The model curves match the fitted values for the mode amplitude and libration phase obtained from fits to selected time intervals shown in Fig. 16 reasonably well.

is reflected. A reasonable approximation is to set

$$\Gamma = n_r/2 + \Gamma_0, \quad (15)$$

where  $n_r$  is the number of radial nodes of the mode between  $a_{\text{res}}$  and the edge of the ring and the constant term  $\Gamma_0 \approx 1/8$  (S. Tremaine, personal communication). Note that this implies that the *total phase shift* around one circuit of the cavity is then  $4\pi\Gamma = 2\pi n_r + \pi/2$  plus that due to the ILR reflection. Numerical solutions of the nonlinear wave equation by Longaretti (2023) show that  $\Gamma$  may in fact be closer to  $1/16$  for an isolated nodeless mode, but that inter-mode interactions may lead to an effective value closer to  $1/8$  for  $m \neq 1$ . For  $m = 1$ , on the other hand, such nonlinear interactions are negligible and a value of  $1/16$  is probably more appropriate. For  $m \neq 1$ , then, we assume  $\Gamma = 1/8$  for the nodeless mode while  $\Gamma = 5/8$  for  $n_r = 1$ , and  $\Gamma = 9/8$  for  $n_r = 2$ , etc. For  $m = 1$ , the corresponding sequence is  $\Gamma = 1/16, 5/16, 9/16$ , etc.

In order to identify the appropriate value of  $n_r$ , and thus  $\Gamma$ , for each mode, we follow Longaretti (2023) and make the simple assumption<sup>7</sup> that, for each value of  $m$ , the mode with the smallest value of  $\Delta a_{\text{res}}$

<sup>7</sup> This assumption is consistent with our interpretation here that all identified librations actually represent trapped edge modes with different numbers of radial nodes.

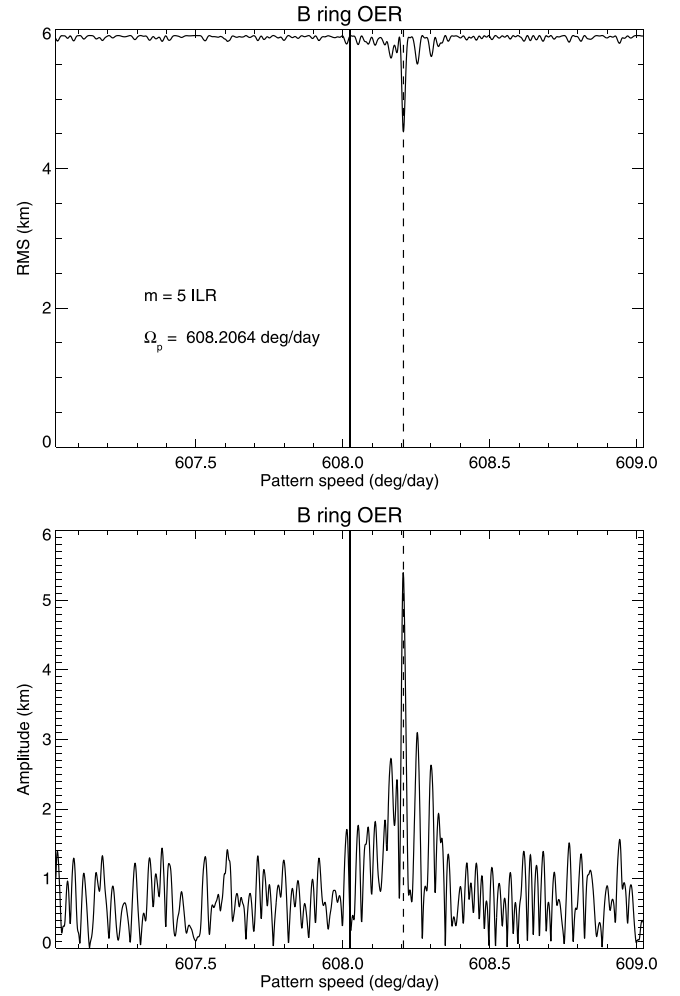


Fig. 18. A scan in pattern speed for  $m = 5$  normal modes, after removing the signatures of all other modes listed in Table 2. The format is the same as Fig. 3. Here the maximum power is seen at one frequency, at  $608.21^\circ \text{ d}^{-1}$ , with a radial amplitude of 5.4 km and a minimum  $\sigma = 4.5$  km.

(i.e., the one whose resonant radius is nearest to the outer edge of the B ring) corresponds to  $n_r = 0$ , with larger values of  $\Delta a_{\text{res}}$  being assigned values of  $n_r = 1, 2$ , etc. Eq. (14) is then used to estimate the average surface mass density within the corresponding resonant cavity, with the results listed in Table 4. We list here the  $m$ -values, the assumed number of radial nodes  $n_r$ , amplitudes, pattern speeds, resonance radii, and implied surface mass densities  $\Sigma$  for all the normal modes identified in this way. The index  $j = 0, 1, \dots$  ranks the modes for each wavenumber in order of decreasing fitted amplitude, with the largest amplitude mode corresponding to  $j = 0$ . For the nodeless modes with  $m > 1$ , we find that the data are fairly well fitted with  $\Sigma \approx 100 \text{ g cm}^{-2}$ , as indicated by the black curve in Fig. 23. (Note that if we were to assume that  $\Gamma_0 = 1/16$  then this estimate would be doubled to  $\sim 200 \text{ g cm}^{-2}$ .) The anomalously large value of  $\Sigma$  in Table 4 for  $m = 5$  and  $n_r = 0$  might be explained if the nodeless mode is too weak to detect and the correct identification here is  $n_r = 1$ , for which we would obtain  $\Sigma \approx 40 \text{ g cm}^{-2}$ . Of course, such a solution implies that many possible modes are too weak to be detected. We will come back to this point shortly.

As discussed in more detail by Longaretti (2023), however, several features of these results suggest that our hypothesis that the observed librations are due to multiple normal modes with the same value of  $m$  but varying numbers of radial nodes  $n_r$  may be incorrect, at least for  $m \neq 1$ . First is the large scatter in the derived surface mass densities

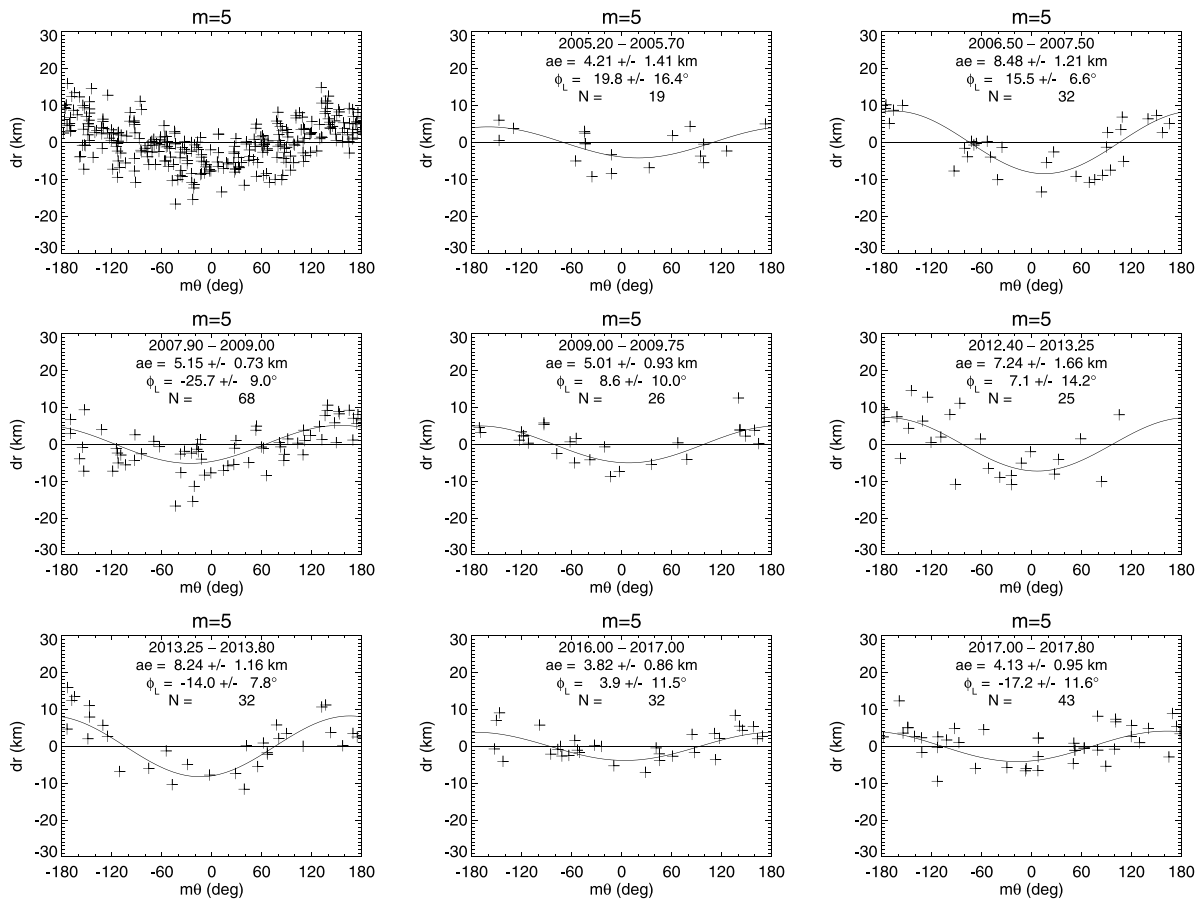


Fig. 19. Radius residuals from our final B ring model when the  $m = 5$  terms are set to zero, plotted as a function of  $m\theta$ , where  $\Omega_p = 608.20674^\circ \text{ d}^{-1}$ . The upper left panel shows the full set of observations. The observations are divided into eight different time intervals in the remaining panels, which show modest variations in the amplitude and phase of the  $m = 5$  pattern over time. See text for details of the model fit results included in these panels.

Table 4  
Normal mode cavities and B ring surface densities.

Mode $m$	$n_r^a$	$j$	$A_m$ (km)	$\Omega_{L,j}$ ( $^\circ \text{ d}^{-1}$ )	$\Omega_{p,j}^b$ ( $^\circ \text{ d}^{-1}$ )	$a_{\text{res}}^c$ (km)	$\Delta a_{\text{res}}^d$ (km)	$\Sigma^e$ ( $\text{g cm}^{-2}$ )	$\Gamma$
1	0	0	23.56		5.0824	117419.9	-150.6	61.9	1/16
	1	1	4.42	0.1145	5.1969	116691.6	-878.9	432.2	5/16
	2	2	2.84	0.1671	5.2495	116364.0	-1206.5	457.5	9/16
2	0	1	37.59	0.1838	382.0763	117537.2	-33.3	101.9	1/8
	0	1	7.41	-0.0500	507.6966	117544.9	-25.6	119.5	1/8
	1	0	11.19		507.7133	117542.3	-28.1	28.9	5/8
3	2	2	2.15	0.1342	507.7580	117535.5	-35.0	24.8	9/8
	0	1	2.79	-0.2032	570.4775	117551.5	-19.0	98.7	1/8
	1	0	7.32		570.5283	117544.5	-25.9	36.7	5/8
4	2	2	2.56	0.1676	570.5702	117538.8	-31.7	30.4	9/8
	0	0	5.42		608.2067	117547.0	-23.5	200.3	1/8
	1	1	1.55	0.4353	608.2938	117535.9	-34.6	87.1	5/8

<sup>a</sup>Number of radial nodes.

<sup>b</sup>Fitted pattern speed:  $\Omega_p$  for  $n_r = 0$  mode and  $\Omega_m = \Omega_p + \Omega_{L,j}/m$  for libration components (see Table 3).

<sup>c</sup>Calculated resonance radius.

<sup>d</sup>Cavity width, based on a mean edge radius of  $a_B = 117570.48$  km.

<sup>e</sup>Ring surface density (see text).

within 40 km of the ring edge, ranging from  $\sim 25$  to over  $100 \text{ g cm}^{-2}$ .<sup>8</sup> This scatter might be explained, at least in part, by a rapid increase in

<sup>8</sup> These estimates may be compared with the surface mass density in the outer B ring obtained by Hedman and Nicholson (2016) of  $\sim 120$ – $140 \text{ g cm}^{-2}$ , from the Janus 3:2 resonance near 116,100 km, and the Lissauer et al. (1985) result of  $54 \text{ g cm}^{-2}$  from the Mimas 4:2 bending wave near 116,500 km,

surface density within 20–30 km of the ring edge, where most of the very large values of  $\Sigma$  occur, but upon closer inspection this does not seem entirely satisfactory, as very different values are found for similar values of  $\Delta a_{\text{res}}$ . In the case of the  $m = 1$  mode, on the other hand, the

although we note that both results apply to regions 1000–1500 km interior to the ring edge, well inside the region occupied by the normal mode cavities.

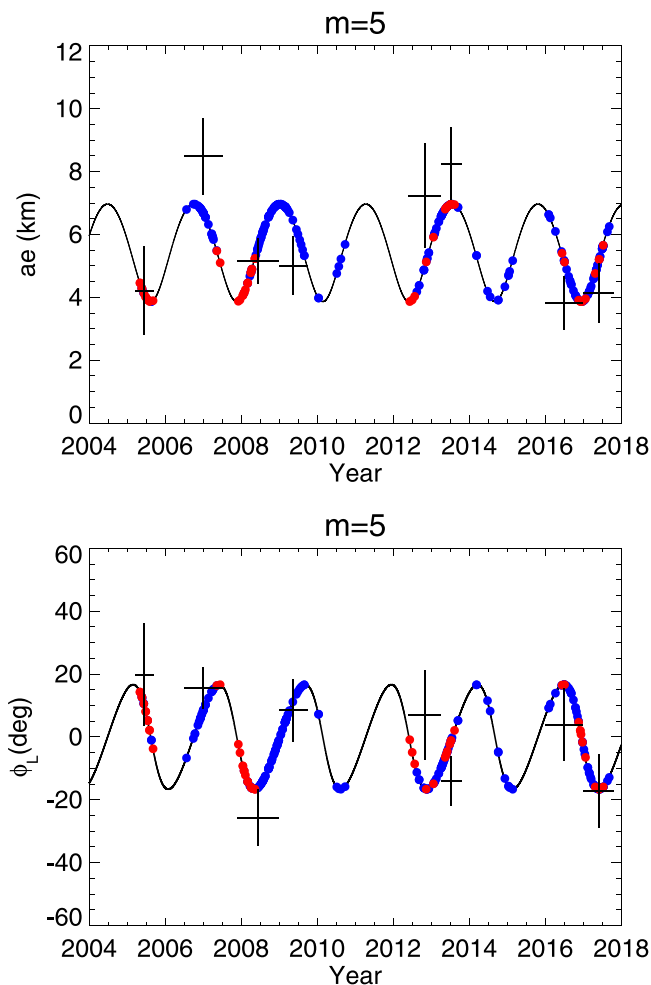


Fig. 20. The modeled variation in the  $m = 5$  amplitude  $A_5$  and phase  $\phi_L$ , along with fitted values over selected intervals from Fig. 19. The single libration period is 2.26 yr and the amplitude is 1.6 km.

very large values of  $\Sigma$  obtained for the secondary modes might be due to our assumption that  $n_r = 1$  and 2. In fact, Longaretti (2023) finds that values of  $n_r = 5$  and 10 provide a more consistent fit to these two modes with an assumed surface density far from the ring edge of  $\Sigma = 60 \text{ g cm}^{-2}$ .

A more serious problem is the very close spacing between modes with different numbers of radial nodes, except for  $m = 1$ , which is much less than would be expected from Eq. (14) and  $\Sigma \approx 100 \text{ g cm}^{-2}$  (cf. the red and blue curves in Fig. 23). Here, choosing larger values of  $n_r$  for the secondary modes would just make the problem worse. We have found no plausible solution to this quandary, unless *all* of the modes with  $m \neq 1$  that we have identified have values of  $n_r \gg 1$ . But in this case, we would need to account for the apparent lack of modes with smaller numbers of radial nodes, which numerical simulations (Longaretti, 2023) suggest should have larger amplitudes.

This brings us to our third concern, which is that numerical models (Longaretti, 2018, 2023) indicate that the secondary mode amplitudes should decrease with increasing numbers of radial nodes, or resonant distance from the ring edge, assuming they have similar values of the maximum dimensionless eccentricity gradient. This is inconsistent with our radial node assignments for  $m = 3$  and  $m = 4$ , although it is possible that inter-mode coupling via the ring's self-gravity could induce oscillations in their amplitudes, resulting in some modes being unusually weak at certain times (Longaretti, 2023).

Summing up the above discussion, it appears that most of the features tentatively identified as nodeless modes in Table 4 can indeed

be interpreted as actual trapped edge modes. In particular, for  $m \neq 1$  their resonant cavity size is consistent with a surface mass density close to the ring edge of  $\sim 100 \text{ g cm}^{-2}$ , except possibly for  $m = 5$ . The  $m = 1$  mode, on the other hand, probes the region further from the edge (up to several hundreds of km rather than a few tens of km) and yields a significantly lower mean surface density of  $\sim 60 \text{ g cm}^{-2}$ , more in line with previous estimates for the B ring derived from density and bending waves. But we note that this difference in surface density does not seem to be mirrored by a similar difference in normal optical depth, although it is consistent with the large variations in ring opacity ( $\tau/\Sigma$ ) at optical depths of order unity found by Hedman and Nicholson (2016).

This leaves open the nature of the  $m \neq 1$  mode librations. Two alternative options are discussed in detail by Longaretti (2023). In brief, the first is that the various oscillations associated with a given  $m$  are in fact overstable librations of the nodeless mode. Alternatively, the oscillations may result from nonlinear non-resonant couplings between the nodeless trapped modes (and possibly other modes with amplitudes too small to have been detected in the data so far). In this regard, the similarity of the libration frequencies  $\Omega_{L,2}$  for  $m = 1$  ( $0.1671^\circ \text{ d}^{-1}$ ) and  $m = 4$  ( $0.1676^\circ \text{ d}^{-1}$ ) to each other, and not far from  $\Omega_{L,0} = 0.1838^\circ \text{ d}^{-1}$ , may be indications of such cross-coupling between modes of different wavenumbers.

We close this section with a few words about the  $m = 2$  mode forced by Mimas. The resonant cavity depth of this mode results from the edge confinement (or torque balance) requirement, and cannot be used to constrain the surface density of the ring as was done above for the free modes. However, the amplitude of this forced mode is determined by a combination of the forcing by Mimas and the ring surface density, which together can be used to derive an independent constraint on the ring's surface mass density close to the edge (within, say, 10–20 km). This leads to a surface density estimate of  $\sim 220 \text{ g cm}^{-2}$  when neglecting the presence of other modes, or about half that value when these additional modes are taken into account (see Longaretti 2023 for details). This result is in reasonable agreement with that derived from the analysis of the free nodeless trapped modes described above.

## 7.2. The phase offset relative to Mimas and the B ring's viscosity

In our reference fit to the Cassini data set in Table 2, the first  $m = 2$  component represents the forced perturbation due to the Mimas 2:1 ILR. This part of the overall model thus contains the primary information on the response of the streamlines at the edge of the B ring to the forcing by the resonance, including any offset in the phase of the response relative to the forcing function. The latter is a predicted consequence of collisional dissipation within the ring, and the size of the phase lag is related to the effective viscosity of the rings (Borderies et al., 1982). Moreover, the amplitude of the torque exerted by Mimas on the rings due to the 2:1 resonance is also dependent on this phase lag (Tajeddine et al., 2017; Longaretti, 2018). Previous investigations have yielded somewhat inconsistent results on the phase lag at the edge of the B ring, ranging from  $2.9 \pm 0.3^\circ$  (Spitale and Porco, 2010) to  $0.7 \pm 1.1^\circ$  in longitude (Nicholson et al., 2014a). In both cases, one of the two minima in ring radius was found to lag behind the mean longitude of Mimas at the epoch of the fit. In this section we compare both the pattern speed and phase of the  $m = 2$  forced perturbation to previous results and to that expected from dynamical theory.

We first compare the measured pattern speed of the forced component of the  $m = 2$  mode with the mean angular velocity of Mimas, as these are expected to be equal (Goldreich and Tremaine, 1978; Porco et al., 1984). The upper panel of Fig. 24 compares the best-fitting pattern speed  $\Omega_p = 381.98430 \pm 0.00045^\circ \text{ d}^{-1}$  of this mode from our reference fit in Table 2 with the actual mean motion of Mimas during

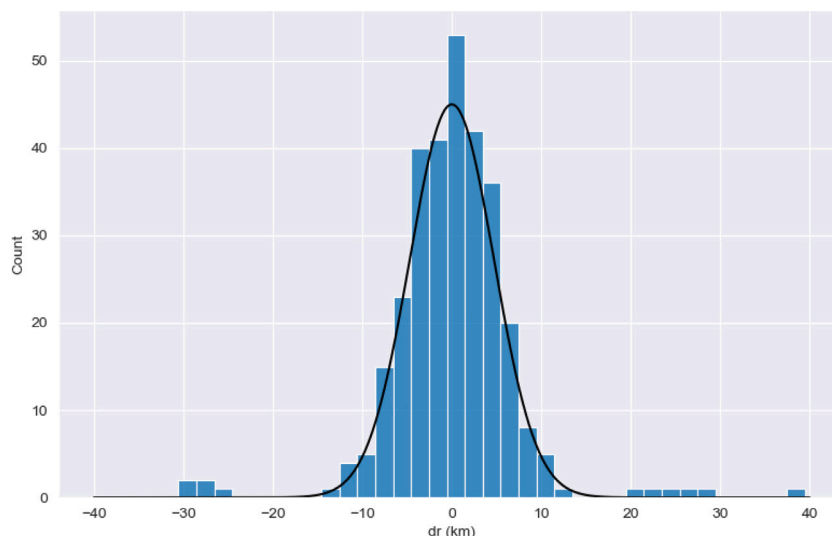


Fig. 21. Histogram of residuals to the final fit, overplotted with a normal distribution with  $\sigma = 4.7$  km. The 11 outlier points with  $|dr| > 20$  km were zero-weighted in the fit.

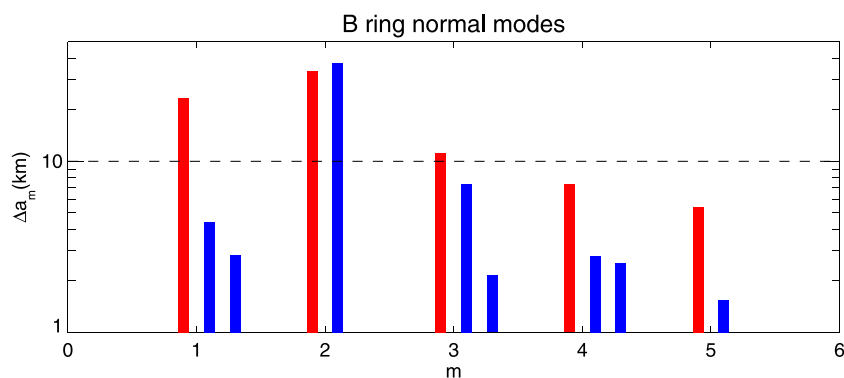


Fig. 22. Histogram of fitted normal modes. Red bars represent the principal mode amplitudes  $ae_0$ , while blue bars show the amplitudes of the libration terms  $ae_j$ . Note that for  $m = 2$ ,  $ae_1$  is larger than  $ae_0$ , the resonantly-forced mode, indicating that the mode is circulating, rather than librating, with respect to Mimas. (For interpretation of the references to color in this figure legend, the reader is referred to the web version of this article.)

the period of the *Cassini* mission, obtained by evaluating the epicyclic orbital elements for the numerical ephemeris, SAT441 (Acton, 1996).<sup>9</sup>

Complicating this comparison is the fact that Mimas itself is in a 4:2 inclination resonance with the satellite Tethys, which leads to long-term periodic variations in the former's longitude, and thus in its mean motion. The libration period of the Mimas–Tethys resonance is  $P_L = 70.8$  yr and the corresponding variations in Mimas's mean longitude have an amplitude of  $\Theta_L = 43.7^\circ$  (Harper and Taylor, 1993). As a result, the satellite's mean motion varies periodically by up to  $2\pi\Theta_L/P_L = 0.0106^\circ \text{ d}^{-1}$ . The long-term average value of  $n_{\text{Mimas}}$  is  $381.994509^\circ \text{ d}^{-1}$ , but in the early part of the *Cassini* mission it was  $\sim 381.9835^\circ \text{ d}^{-1}$ , near its minimum value (Nicholson et al., 2014a). The long-term trend in Mimas's mean motion seen in Fig. 24 is a consequence of this slow variation. In addition to the long-term trend, there is a shorter-term variation in the epicyclic mean motion with a period of 0.62 yr and an amplitude of  $\pm 0.005^\circ \text{ d}^{-1}$  that is associated with the nearby 2:1 Lindblad resonance with Tethys (Vienne and Duriez, 1995). These variations in

the mean motion of Mimas make an instantaneous comparison with the fitted pattern speed of the forced  $m = 2$  perturbation rather tricky, but Fig. 24 shows that the best-fitting pattern speed is indeed very close to the average mean motion of Mimas during the period of our observations.

Having established that the forced  $m = 2$  mode closely tracks the average mean motion of Mimas, the next step is to measure the offset in phase between the radial minimum of the mode and the average longitude of Mimas. This is also complicated by the effects of the Mimas–Tethys resonance. We make the working assumption that the ring is able to follow the slow librational motion of Mimas's longitude, but not the short-period variations in its true or instantaneous longitude. Our approach therefore is to remove the short-period variations by subtracting from the epicyclic mean longitude a linear term with a rate of  $381.9842959^\circ \text{ d}^{-1}$ , as determined from our reference fit in Table 2. The lower panel in Fig. 24 compares the fitted phase of the forced  $m = 2$  mode, which uses this same pattern speed, with Mimas's detrended orbital longitude from the numerical ephemeris. In addition, a constant offset equal to Mimas's epicyclic mean longitude at our reference time of 2008 Jan 1 12:00 UTC, or  $347.21996^\circ$ , has been subtracted from both the Mimas longitudes and the fitted  $m = 2$  phase. The short vertical line marks this epoch. By construction, the detrended Mimas mean longitude is exactly zero at our reference time, although the long-period resonant variations are still apparent, especially after 2015. The best-fitting value of the phase lag from the reference fit in Table 2 is  $-0.39 \pm 0.73^\circ$  relative to the epicyclic longitude of Mimas at

<sup>9</sup> The epicyclic elements are analogous to the usual osculating Keplerian orbital elements, but take into account the zonal gravity coefficients of the planet ( $J_2$ ,  $J_4$ , etc.) that have the effect of modifying Kepler's third law and introducing precession of both the apsidal line and the nodes of eccentric or inclined orbits. See Borderies-Rappaport and Longaretti (1994) and Renner and Sicardy (2006) for further details and conversion formulae from osculating to epicyclic elements.

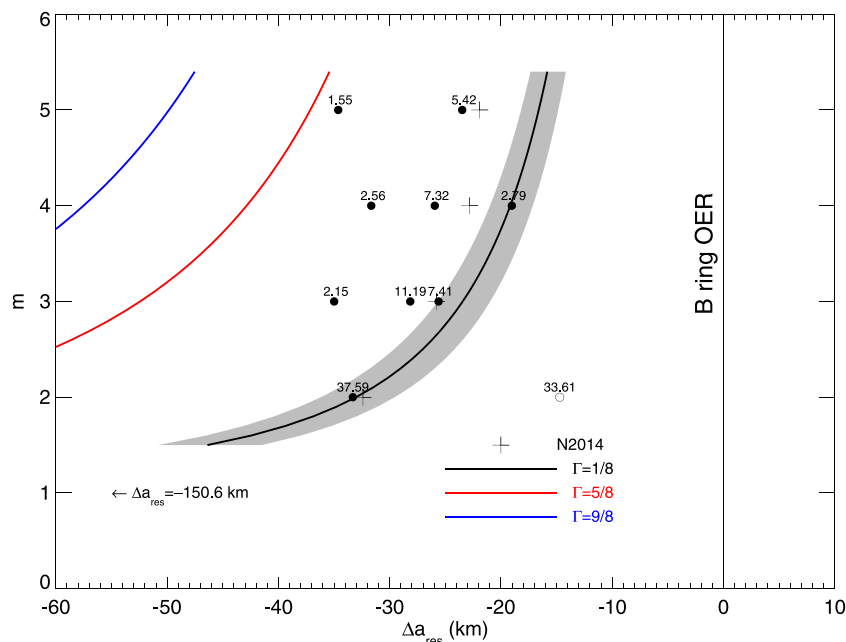


**Fig. 23.** The locations of the calculated resonance radii  $a_{\text{res}}$  for normal modes with  $m = 2, 3, 4$  and  $5$  relative to the mean radius of the outer edge of the B ring, on the assumption that the fitted mode librations represent beating between normal modes with different numbers of radial nodes  $n_r$ . Free modes are plotted as filled circles; the open circle marks the  $m = 2$  mode forced by Mimas. The amplitude of each fitted mode (in km) is listed next to each point. The black curve shows the predicted value of  $\Delta a_{\text{res}}$  as a function of  $m$  for nodeless modes (i.e., those with  $n_r = 0$ ), a surface mass density  $\Sigma = 100 \text{ g cm}^{-2}$  and  $\Gamma = 1/8$  (see text). The gray shaded region bounds the range  $\Sigma = 80\text{--}120 \text{ g cm}^{-2}$ , from right to left. The red and blue curves show the corresponding values of  $\Delta a_{\text{res}}$  predicted for normal modes with  $n_r = 1$  and  $2$ , respectively. With the exception of  $m = 1$  and  $m = 5$ , the lowest-frequency mode for each value of  $m$  is roughly consistent with  $\Sigma \approx 100 \text{ g cm}^{-2}$ . (For the primary  $m = 1$  mode,  $\Delta a_{\text{res}} = -150.6 \text{ km}$  and is off-scale, reflecting the much longer radial wavelengths of the associated density waves.) For comparison, the estimates of  $\Delta a_{\text{res}}$  for these same modes from [Nicholson et al. \(2014a\)](#) are shown by the + symbols. (For interpretation of the references to color in this figure legend, the reader is referred to the web version of this article.)

the reference time, as shown by the horizontal blue line in [Fig. 24](#). If instead we use our final fit from [Table 3](#), for which  $\delta = 346.10 \pm 0.59^\circ$ , we find an offset of  $-1.12 \pm 0.59^\circ$  relative to Mimas. These results are consistent with the less-precise phase lag of  $-0.7 \pm 1.1^\circ$  found by [Nicholson et al. \(2014a\)](#), but somewhat smaller in magnitude than that obtained by [Spitale and Porco \(2010\)](#), viz.  $-2.3 \pm 0.3^\circ$ .

Given the departures of Mimas's epicyclic longitude from any constant-rate model, one might ask if there is a better way to measure the true phase offset. One alternative is to use the actual epicyclic mean longitude of Mimas in the orbit fitting program, instead of the linear term in [Eq. \(1\)](#), and then solve for a constant offset with respect to this, which we refer to as  $\delta\lambda$  — this was the approach followed by [Nicholson et al. \(2014a\)](#). We have repeated both our reference fit in [Table 2](#) and our final fit ([Table 3](#)) with this modification. We find that  $\delta\lambda = -0.51 \pm 0.56^\circ$  and  $-1.28 \pm 0.38^\circ$ , respectively. Within their uncertainties, all four estimates of the phase lag are reasonably consistent and imply a small negative offset in the longitude of one minimum of the forced  $m = 2$  mode relative to the mean epicyclic longitude of Mimas. As discussed in [Nicholson et al. \(2023\)](#), such a phase lag in the radial minimum is consistent with a gravitational torque between Mimas and the rings that acts to remove excess angular momentum from the B ring and transfers it to the satellite. But we must caution the reader that the measured phase lag is only barely statistically significant, and might also be subject to significant temporal variations associated with the observed mode librations ([Longaretti, 2018](#)).

The present and previously published estimates of the phase lag of the forced  $m = 2$  mode with respect to Mimas's mean longitude can be used to constrain the effective viscosity within the last few tens of km of ring's outer edge. On the other hand, the surface mass density  $\Sigma \sim 60 \text{ g cm}^{-2}$  obtained from the analysis of the  $m = 1$  normal mode also indirectly constrains the ring's viscosity under the plausible assumption that angular momentum transport in this wider region (up to 1000 km from the ring edge) is dominated by self-gravity wakes ([Daisaka et al., 2001](#)), although numerical simulations suggest that wake formation in

the B ring may be limited for such a low value of  $\Sigma$  ([Robbins et al., 2010](#)). As shown in detail by [Longaretti \(2023\)](#), these two estimates of the ring viscosity at different distances from the edge are consistent with one another, once the substantial increase in dissipation produced by the confinement of the edge by Mimas is taken into account, leading to a viscosity far from the ring edge of  $\nu_0 \approx 5\text{--}15 \text{ cm}^2 \text{ s}^{-1}$ .

## 8. Conclusions and open questions

- The dominant  $m = 2$  mode at the outer edge of the B ring is observed to circulate with a period of 5.36 yr and an amplitude that varies from a minimum of 4 km to a maximum of 71 km. Under the assumption that this is due to a combination of a resonantly-forced perturbation by Mimas plus an  $m = 2$  normal mode ([Spitale and Porco, 2010](#); [Nicholson et al., 2014a](#)), we find  $\Delta a_{\text{res}} = -14.7 \text{ km}$  and  $A_m = 33.6 \text{ km}$  for the forced mode, while  $\Delta a_{\text{res}} = -33.3 \text{ km}$  and  $A_m = 37.6 \text{ km}$  for the free mode. The near equality in amplitude of the two modes is intriguing. This may simply be coincidental, but another option is that what we have identified as a free mode is instead an overstable component of the forced mode. The near-equality of amplitude could then be a result of nonlinear saturation of the overstability. If this leads to circulation instead of libration, the two amplitudes must of necessity be nearly the same, since the mean eccentricity for such a mode is similar to the eccentricity gradient across the resonant cavity.
- Additional modes of radial oscillation are seen with azimuthal wavenumbers  $m = 1, 3, 4$  and  $5$  and mean amplitudes ranging from 5 to 24 km, interpreted here as normal modes trapped in resonant cavities at the edge of the B ring. From their observed pattern speeds, we calculate resonant cavity widths  $\Delta a_{\text{res}}$  that range from 151 km for  $m = 1$  to 23 km for  $m = 5$ . A recurrent question here, and also for the edge of the A ring ([Nicholson et al., 2023](#)), is why we see some modes and not others. If modes are

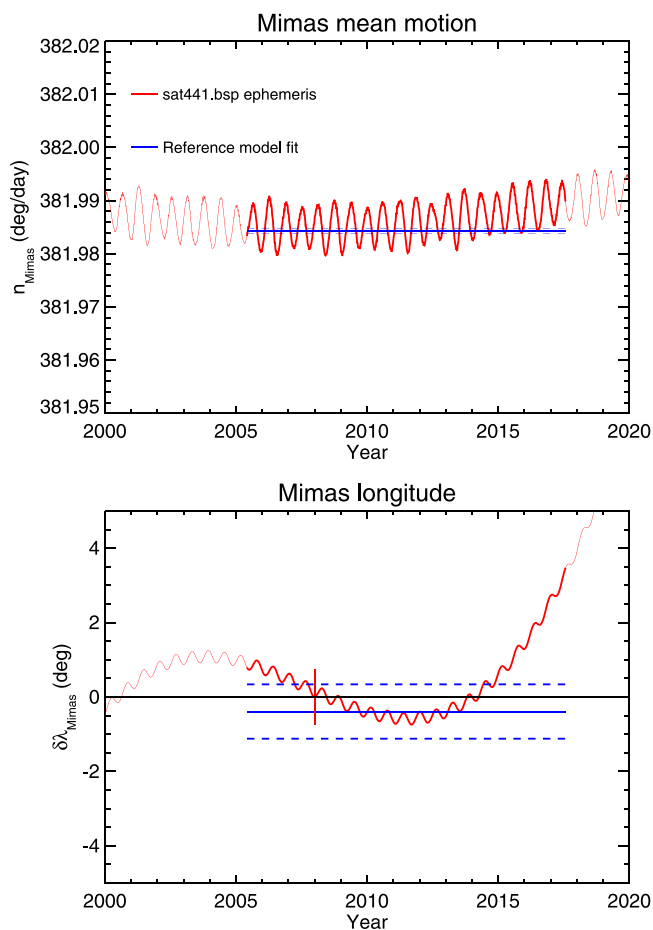


**Fig. 24.** (Upper panel) A comparison of the fitted pattern speed of the forced  $m = 2$  mode with the actual mean motion of Mimas obtained by evaluating the epicyclic orbital elements from the numerical ephemeris SAT441. The horizontal lines show the fitted pattern speed and error bars for the forced mode,  $\Omega_p$ , from our reference fit in Table 2, while the oscillatory curve is from the satellite ephemeris. (Lower panel) A comparison of the fitted phase  $\delta$  of the forced  $m = 2$  mode from the reference fit with the mean longitude of Mimas at  $t = t_0$  derived from the ephemeris. The horizontal line with error bars shows the mode phase relative to Mimas's mean longitude at our reference epoch, while the oscillatory curve is again from the satellite ephemeris. The latter has had a linear trend removed with a slope equal to the best-fitting mode pattern speed shown in the upper panel, and both the mode phase and detrended Mimas longitudes are calculated relative to the mean epicyclic longitude of Mimas at  $t = t_0$ . The short vertical line marks the epoch of the fitted orbital elements, when the measured phase lag was  $-0.39 \pm 0.73^\circ$ . In both panels, the curves computed from the satellite ephemeris are plotted as heavier lines during the actual period of *Cassini* observations used in the fits.

maintained by a viscous overstability, then in principle modes with all values of  $m$  may be excited. However, such modes will necessarily undergo nonlinear non-resonant couplings, leading to quasi-periodic time-variation of the mode amplitudes. They may not have detectable amplitudes at all times, and the amplitude distribution may well appear to be chaotic.

- It appears that the unforced modes with  $m = 1, 3, 4$  and  $5$  all librate in amplitude and phase, and, except for  $m = 5$ , each mode appears to exhibit at least two libration terms. Libration amplitudes range from 1.6 to 7.4 km and the periods  $2\pi/\Omega_L$  range from 2.3 to  $\sim 20$  yr, with an average of  $\sim 6$  yr. From the shape of the ring edge alone, we cannot discriminate between three possible dynamical explanations for the librations: (1) true physical oscillations of the amplitudes and phases of normal modes, possibly due to a viscous overstability; (2) apparent oscillations due to the beating of separate normal modes with the same

value of  $m$  but different numbers of radial nodes; or (3) quasi-periodic changes in amplitude and phase on decadal timescales as a consequence of nonlinear and non-resonant coupling between excited modes with different values of  $m$ .

- Under the assumption that dynamical model (2) above is correct, we use the resonant cavity widths of the various modes to estimate the surface mass density  $\Sigma$  in the outermost parts of the B ring. For the nodeless modes (*i.e.*, those with  $n_r = 0$ ) with  $m \neq 1$  we find that  $\Sigma \approx 100 \text{ g cm}^{-2}$ , while for the  $m = 1$  mode – whose cavity is much wider – we find  $\Sigma \approx 60 \text{ g cm}^{-2}$ . These results are consistent with those derived previously from the few density and bending waves identified in the B ring (Hedman and Nicholson, 2016). However, modes with non-zero numbers of radial nodes typically yield much lower values of  $25\text{--}35 \text{ g cm}^{-2}$ , suggesting that a different model is necessary to account for these features.
- Given the large amplitude of the  $m = 2$  mode, and the resulting substantial eccentricity gradient  $q$  in the outer B ring, one might expect the existence of overtone modes, with perturbations varying as an  $n$ -tuple of  $m[\lambda - \Omega_p(t - t_0) - \delta]$ . Such distortions should look like normal modes with  $m' = nm$  but the same pattern speed  $\Omega_p$ . A search has not revealed any evidence for such modes with  $m = 4$  or  $m = 6$  and  $\Omega_p = \Omega_2$ .
- Despite careful searches, no additional long-lived modes have been identified for values of  $m > 5$ , or for negative values of  $m$ . (The latter would correspond to OLR-type modes that are not expected to exist at outer ring edges.)
- The overall rms residual of our best fit is 4.7 km, at least 10 times larger than the uncertainties in the measured radii and much greater than the residuals obtained for fits to other sharp-edged features in the nearby Cassini Division (French et al., 2016). Possible explanations range from additional unmodeled global modes of oscillation to localized distortions such as those seen in some ISS images (Spitale and Porco, 2010; Hedman and Nicholson, 2019). At any given time, a number of weaker modes may be present but with amplitudes that are too small to be individually detected. However, such modes would still contribute to the radius residuals.
- Our analysis of the forced component of the  $m = 2$  mode, and that of Spitale and Porco (2010), indicate that one minimum of the radial pattern lags behind the mean longitude of Mimas by  $1\text{--}2^\circ$ . A more accurate estimate is made difficult by the various long-term perturbations in the orbit of Mimas due to the 4:2 vertical resonance with Tethys ( $P_L = 70$  yr) and the nearby 2:1 Lindblad resonance ( $P_L = 0.62$  yr), but the sign of the lag is consistent with the expectation that Mimas is removing angular momentum from the B ring at the 2:1 resonance, and thus preventing it from spreading due to viscous interactions.
- An analysis of the phase lag of the forced mode in a companion paper by Longaretti (2023) yields an estimate for the kinematic viscosity of the outer B ring, but well inside the perturbed edge, of  $\nu_0 = 5\text{--}15 \text{ cm}^2 \text{ s}^{-1}$ , compatible with the expectation that self-gravity wakes dominate the outward transport of angular momentum in this region.

#### Declaration of competing interest

The authors declare that they have no known competing financial interests or personal relationships that could have appeared to influence the work reported in this paper.

#### Data availability

Data will be made available on request.

## Acknowledgments

We appreciate the helpful comments of the two anonymous referees. This work was supported in part by the Cassini project and by NASA CDAP grants NNX09SE66G and 80NSSC10K0890. P.Y.L. acknowledges support by the French National Program of Planetology (PNP). We thank Peter Goldreich for many conversations about the complex dynamics of ring edges. We are especially grateful to Aseel Anabtawi for her leadership of the *Cassini* RSS Operations Team, and to all at JPL and the NASA DSN and ESA ground stations who supported the successful two-way RSS occultation experiments used for this work.

## References

- Acton, C.H., 1996. Ancillary data services of NASA's navigation and ancillary information facility. *Planet. Space Sci.* 44, 65–70.
- Borderies, N., Goldreich, P., Tremaine, S., 1982. Sharp edges of planetary rings. *Nature* 299 (209).
- Borderies, N., Goldreich, P., Tremaine, S., 1985. A granular flow model for dense planetary rings. *Icarus* 63, 406–420.
- Borderies-Rappaport, N., Longaretti, P.-Y., 1994. Test particle motion around an oblate planet. *Icarus* 107, 129–141. <http://dx.doi.org/10.1006/icar.1994.1011>.
- Daisaka, H., Tanaka, H., Ida, S., 2001. Viscosity in a sense planetary ring with self-gravitating particles. *Icarus* 154, 296–312. <http://dx.doi.org/10.1006/icar.2001.6716>.
- French, R.G., Marouf, E.A., Rappaport, N.J., McGhee, C.A., 2010. Occultation observations of Saturn's B ring and Cassini division. *Astron. J.* 139, 1649–1667.
- French, R.G., McGhee-French, C.A., Lonergan, K., Sepersky, T., Jacobson, R.A., Nicholson, P.D., Hedman, M.M., Marouf, E.A., Colwell, J.E., 2017. Noncircular features in saturn's rings IV: Absolute radius scale and saturn's pole direction. *Icarus* 290, 14–45.
- French, R.G., Nicholson, P.D., McGhee-French, C.A., Lonergan, K., Sepersky, T., Hedman, M.M., Marouf, E.A., Colwell, J.E., 2016. Noncircular features in saturn's rings III: The cassini division. *Icarus* 274, 131–162.
- French, R.G., Nicholson, P.D., Porco, C.C., Marouf, E.A., 1991. Dynamics and structure of the uranian rings. In: *Uranus*. Univ. Arizona Press, p. 327.
- Goldreich, P., Tremaine, S.D., 1978. The formation of the cassini division in saturn's rings. *Icarus* 34, 240–253.
- Harper, D., Taylor, D.B., 1993. The orbits of the major satellites of saturn. *Astron. Astrophys.* 268 (326).
- Hedman, M.M., Nicholson, P.D., 2016. The B-ring's surface mass density from hidden density waves: Less than meets the eye? *Icarus* 279, 109–124.
- Hedman, M.M., Nicholson, P.D., 2019. Axisymmetric density waves in Saturn's rings. *Mon. Not. R. Astron. Soc.* 485, 13–29.
- Hedman, M.M., Nicholson, P.D., Baines, K.H., Buratti, B.J., Sotin, C., Clark, R.N., Brown, R.H., French, R.G., Marouf, E.A., 2010. The architecture of the cassini division. *Astron. J.* 139, 228–251.
- Kirkwood, D., 1866. On the theory of meteors. *Proc. Am. Assoc. Adv. Sci.* 8–14.
- Lissauer, J.J., Goldreich, P., Tremaine, S., 1985. Evolution of the janus-epimetheus coorbital resonance due to torques from Saturn's ring. *Icarus* 64 (425).
- Longaretti, P.-Y., 2018. Theory of narrow rings and sharp edges. In: *Planetary Ring Systems: Properties, Structure, and Evolution*. Cambridge University Press, pp. 225–275.
- Longaretti, P.-Y., 2023. Stationary dynamics of planetary ring edge modes. I Saturn's B edge. *Icarus* (in preparation).
- Marouf, E.A., Tyler, G.L., Rosen, P.A., 1986. Profiling saturn's rings by radio occultation. *Icarus* 68 (120).
- Murray, C.D., Dermott, S.F., 1999. *Solar System Dynamics*. Cambridge University Press.
- Nicholson, P.D., French, R.G., colleagues, 11, 2023. The seven-lobed shape of the outer edge of saturn's a ring. *Icarus* 390, 115287. <http://dx.doi.org/10.1016/j.icarus.2022.115287>.
- Nicholson, P.D., French, R.G., Hedman, M.M., Marouf, E.A., Colwell, J.E., 2014a. Noncircular features in saturn's rings: I. The edge of the b ring. *Icarus* 227, 152–175.
- Nicholson, P.D., French, R.G., McGhee-French, C.A., Hedman, M.M., Marouf, E.A., Colwell, J.E., Lonergan, K., Sepersky, T., 2014b. Noncircular features in saturn's rings: II. The C ring. *Icarus* 241, 373–396.
- Nicholson, P.D., French, R.G., Spitale, J.N., 2018. Narrow Rings, Gaps, and Sharp Edges. *Planetary Ring Systems: Properties, Structure, and Evolution* Cambridge Univ. Press, pp. 276–307.
- Porco, C., Danielson, G.E., Goldreich, P., Holberg, J.B., Lane, A.L., 1984. Saturn's nonaxisymmetric ring edges at 1.95 R(s) and 2.27 R(s). *Icarus* 60, 17–28.
- Renner, S., Sicardy, B., 2006. Use of the geometric elements in numerical simulations. *Celestial Mech. Dynam. Astronom.* 94 (237).
- Robbins, S.J., Stewart, G.R., Lewis, M.C., Colwell, J.E., Sremčević, M., 2010. Estimating the masses of saturn's A and B rings from high-optical depth N-body simulations and stellar occultations. *Icarus* 206, 431–445. <http://dx.doi.org/10.1016/j.icarus.2009.09.012>.
- Schinder, P.J., colleagues, 6., 2015. A numerical technique for two-way radio occultations by oblate axisymmetric atmospheres with zonal winds. *Radio Sci.* 50 (712).
- Spitale, J.N., Porco, C.C., 2009. Time variability in the outer edge of saturn's A-ring revealed by cassini imaging. *Astron. J.* 138, 1520–1528.
- Spitale, J.N., Porco, C.C., 2010. Detection of free unstable modes and massive bodies in saturn's outer B ring. *Astron. J.* 140, 1747–1757.
- Tajeddine, R., Nicholson, P.D., Longaretti, P.-Y., El Moutamid, M., Burns, J.A., 2017. What confines the rings of Saturn? *Astrophys. J. Suppl. Ser.* 232, 28.
- Tiscareno, M.S., Harris, B.E., 2018. Mapping spiral waves and other radial features in Saturn's rings. *Icarus* 312, 157–171.
- Vienne, A., Duriez, L., 1995. TASS1.6: Ephemerides of the major saturnian satellites. *Astron. Astrophys.* 297, 588–605.